

APPROVAL SHEET

Title of Thesis: Application of the rigorous coupled-wave algorithm to impedance-matched metal-dielectric metamaterials with moth-eye surfaces.

Name of Candidate: Rushin Contractor,
Master of Science, 2018.

Thesis and Abstract Approved: _____
Dr. Curtis Menyuk,
Professor,
Computer Science and
Electrical Engineering Department.

Date Approved: _____

Curriculum Vitae

Name: Rushin Manan Contractor

Permanent Address: 19559 Taverney Dr, Gaithersburg, MD 20879

Degree and date to be conferred: MS, 05/2018

Date of Birth: 09/02/1992

Place of Birth: Ahmedabad, India

Secondary Education: St. Xavier's High School, Loyola Hall,
Ahmedabad, Gujarat, India.

Collegiate institutions attended:

University of Maryland Baltimore County, M.S. Electrical Engineering, 2018.
Indian Institute of Technology Roorkee, B.Tech Electrical Engineering, 2014.

Major: Electrical Engineering

Professional publications:

Professional positions held:

Network Specialty Group,
610 Professional Dr., Gaithersburg, MD 20879.
(08/2015 – present)

ABSTRACT

Title of Thesis: APPLICATION OF THE RIGOROUS COUPLED-WAVE ALGORITHM TO IMPEDANCE-MATCHED METAL-DIELECTRIC METAMATERIALS WITH MOTH-EYE SURFACES.

Rushin Contractor, Master of Science, 2018.

Thesis directed by: Dr. Curtis Menyuk, Professor,
Computer Science and Electrical Engineering Department.

This thesis contains the theoretical basis for the rigorous coupled-wave algorithm (RCWA) and its application to the design of novel materials with desired electromagnetic properties. The RCWA is typically used to calculate diffraction efficiencies and electromagnetic field distribution during the scattering of light by periodic dielectric structures. First, the basic idea of the algorithm is introduced for a single grating layer with unidirectional periodicity [1]. The next chapter covers the stacking of multiple layers of gratings using the scattering matrix [2] and the big matrix method [3]. These ideas are then extended to gratings having periodicity in both orthogonal directions perpendicular to the plane of incidence [4, 5]. The concepts introduced in these independent sources are consolidated using a consistent mathematical framework, and the results produced by the algorithm for several photonic structures are presented. Finally, application of the RCWA to design a new metamaterial with polarization-independent ultra-broadband absorption is discussed.

**APPLICATION OF THE RIGOROUS COUPLED-WAVE
ALGORITHM TO IMPEDANCE-MATCHED
METAL-DIELECTRIC METAMATERIALS WITH
MOTH-EYE SURFACES**

by
Rushin Contractor

Thesis submitted to the Faculty of the Graduate School
of the University of Maryland in partial fulfillment
of the requirements for the degree of
Master of Science
2018

© Copyright by
Rushin Contractor
2018

*To my parents,
Manan and Chetna.*

ACKNOWLEDGMENTS

This thesis is a compilation of the work the I have done to complete my first research problem. It will always hold great significance to me and is only made possible due to contributions from a few very special individuals.

I was only able to step into this position due to tremendous support from my uncle Sunil Contractor, who gave me a home, and who helped me secure a job and admission to UMBC. I would also like to thank my aunt Bela and cousins Parth and Niti for helping me cope with all the little problems that I faced during my first year in this country.

I thank Munir for helping me with finances and for being the ever-caring older brother in my life. My parents, always looking out for me, even from across the globe have been my greatest source of encouragement and kept me going through the toughest of times. A great many trips and conversations with Niel and Shaurya were also instrumental in taking my mind off the combined pressures of a job, college, and research.

Most importantly, I would like to express my sincerest gratitude to Dr. Giuseppe D'Aguanno. He has continuously guided the work presented here and helped me find solutions to the myriad of challenges that I faced during this journey. Even all the way from Texas he was always within arm's reach, lending me his expertise when the results did not look promising. I could never have hoped for a better mentor.

Finally, I would like to thank my advisor Dr. Curtis Menyuk. He made it possible for me to work with Dr. D'Aguanno, and Dr. Menyuk's guidance has helped me immensely improve my technical writing and presentation. These skills will undoubtedly be invaluable throughout my future endeavors.

TABLE OF CONTENTS

DEDICATION	ii
ACKNOWLEDGMENTS	iii
LIST OF FIGURES	vi
Chapter 1 OVERVIEW	1
Chapter 2 SINGLE-LAYERED GRATINGS	5
2.1 The permittivity expansion for binary gratings	5
2.2 TE-polarized incidence	6
2.2.1 Fields in the homogeneous regions	7
2.2.2 Fields in the grating region	8
2.2.3 The eigenvalue problem	10
2.2.4 Boundary conditions	12
2.2.5 Estimating the fields	13
2.2.6 Chalcogenide glass	15
2.3 TM Polarization	16
2.3.1 The classical approach	16
2.3.2 An improved formulation for the TM-polarization	18

2.3.3	Dealing with a complex permittivity: Diffraction in silver gratings	20
Chapter 3	MULTIPLE LAYERS	22
3.1	Lamellarization	22
3.2	Calculating the efficiencies: The S-matrix method	24
3.2.1	Implementing the S matrix for single-layered gratings	26
3.2.2	A generalized approach	27
3.2.3	Results	28
3.3	Fields within the structure: The big matrix approach	28
3.3.1	The big matrix for a single layer	32
3.3.2	The general case	33
3.3.3	Results	34
Chapter 4	3D GRATINGS	36
4.1	Reflected and Transmitted Fields	37
4.2	Fourier transforms of the permittivity function	39
4.3	The Eigenvalue Equation	41
4.4	Fields in 3D	42
Chapter 5	A NOVEL METAMATERIAL ABSORBER	44
5.1	Introduction	44
5.2	Results and Discussion	47
5.3	Conclusion	55
Appendix A	MATLAB SCRIPTS	57

LIST OF FIGURES

1.1	Example of a single layered binary grating [1].	3
2.1	(a) The basic structure of the As_2S_3 grating used to test the algorithm for 1D gratings [6]. Thickness $h = 200$ nm. (b) Reflection resonances for three slit sizes of chalcogenide glass a	15
2.2	(a) D’Aguanno et al. [7, Fig. 1]. The basic geometry of the silver gratings. For this example, we set $D_x = 285$ nm, $a = 32$ nm, and $h = 400$ nm. (b) Transmission spectrum of the gratings where $\omega/\omega_{\text{ref}} = 1/\lambda_0$	21
3.1	The decomposition of a 2D structure into many thin layers [8].	23
3.2	Schematic representation of the S-matrix as a four-port system.	24
3.3	Stacking of two systems represented as S-matrices.	26
3.4	(a) D’Aguanno et al. [9, Fig. 1a]. Structure for the results shown in Figs. 3.5 with the following parameters: number of rows $N_r = 5$, $r/a = 0.2$, $a = 1$ μm , and relative permittivity of columns $\epsilon = 12.5$. (b) Structure for the plots in Figs. 3.6. Correctly labelled version of [9, Fig. 7a] with parameters: $N_r = 5$, $r/a = 0.2$, $\epsilon = 11.4$	29
3.5	Transmission spectrum for TE-polarized incidence on 2D gratings shown in Fig. 3.4a. Reproduction of (a) [9, Fig. 2] and (b) [9, Fig. 1b].	30
3.6	Reproduction of the transmission efficiency plots for TM-polarized incidence on 2D gratings shown in Fig. 3.4b. Compare with (a) [9, Fig. 7c] and (b) [9, Fig. 7b]	30
3.7	Field distribution for the photonic structure in Fig. 3.4a with TE-polarized incidence. Electric field intensity at the Dirac point for (a) normal incidence and for (b) $\theta = 0.1^\circ$	35

3.8	Field distribution for the photonic structure in Fig. 3.4b with TM-polarized incidence. Electric field intensity at the Dirac point for (a) normal incidence and for (b) $\theta = 0.1^\circ$	35
4.1	Schematic representation of a doubly periodic, binary surface-relief grating [4, Fig. 1].	37
5.1	Schematic illustrations of the metamaterials and incidence geometry. (a) Lateral view of impedance matched metal-dielectric metamaterials with a flat surface (left) and moth-eye surface (right). The elementary cell has a period Λ , and it consists of a metal layer of thickness d_M sandwiched between dielectric layers of thickness d_D . For the truncated conical pillars that form the moth-eye surface (right), the variables r_1 and r_2 are the radius at the top and bottom respectively and h is the height of the pillars. The geometry for TE-polarized incidence is also shown. (b) Top and 3D view of moth-eye surfaces obtained by arranging the truncated conical pillars in a triangular lattice with periods D_x and $D_y = \sqrt{3}D_x$ in the x - and y -directions respectively. The polarization angle ϕ is shown here for normal incidence.	46
5.2	The absorption spectrum for the Cu-based metamaterial that we consider with TE-polarized incidence ($\phi = 90^\circ$). The elementary cell in this metamaterial has metal layers of thickness, $d_M = 10$ nm and SiO_2 layers of thickness, $d_D = 30$ nm. The moth-eye surface has a height $h = 280$ nm, periods $D_x = 300$ nm and $D_y = 520$ nm, and radii $r_1 = 50$ nm and $r_2 = 145$ nm.	48
5.3	Same as Fig. 5.2 with TM-polarization ($\phi = 0^\circ$).	49

5.4	The absorption spectrum for the W-based metamaterials that we consider with TE-polarized incidence. Structure parameters, $d_M = 5$ nm, $d_D = 75$ nm, $h = 620$ nm, $D_x = 834$ nm, $D_y = 1444$ nm, $r_1 = 236$ nm, and $r_2 = 383$ nm.	49
5.5	Same as Fig. 5.4 with TM-polarization.	50
5.6	The absorption spectrum for the non-impedance-matched all-metal films and moth-eye structures. (a) Moth-eye surfaces made entirely of Cu with TM-polarized incidence. (b) Moth-eye surfaces made entirely from W with TE-polarized incidence. (c) 700 nm thick Cu-film with TM-polarized incidence. (d) 1550 nm thick W-film with TE-polarized incidence. The dimensions for the moth-eye surfaces are outlined in Fig. 5.2 for (a) and Fig. 5.4 for (b) with a transmission region of the same metal. Transmission region for (c) and (d) is air.	51
5.7	Electric field intensity and ohmic loss distribution for Cu-based metamaterials. (a) $\lambda = 0.5$ μm , absorption $> 99\%$. (b) $\lambda = 0.5$ μm , absorption $\approx 95\%$. (c) $\lambda = 1.2$ μm , absorption $\approx 99\%$. (d) $\lambda = 1.2$ μm , absorption $\approx 20\%$	53
5.8	Electric field intensity and ohmic loss distribution for W-based metamaterials. (a) $\lambda = 2.5$ μm , absorption $\approx 90\%$. (b) $\lambda = 2.5$ μm , absorption $\approx 90\%$. (c) $\lambda = 5$ μm , absorption $> 99\%$. (d) $\lambda = 5$ μm , absorption $\approx 15\%$	54

Chapter 1

OVERVIEW

The rigorous coupled-wave algorithm (RCWA) is a semi-analytical Fourier space method that can be used to find exact solutions for electromagnetic waves that diffract through intricate grating structures. The geometry of such a structure is shown in Fig. 1.1. A unit amplitude, monochromatic plane wave with free space wavelength λ_0 travelling from the half-space $z < 0$ at an arbitrary angle with respect to the z direction, is assumed to be incident on a permittivity distribution that varies along the (x, y) plane with finite thickness h . The regions I & II on either side of the grating layer $0 < z < h$ are homogeneous with refractive indices n_{I} and n_{II} respectively.

The incident electric field from such a plane wave at any point with $z < 0$ can be written as,

$$\mathbf{E}_{\text{inc}}(\mathbf{r}) = \exp(-j\mathbf{k}_{\text{inc}} \cdot \mathbf{r}) \hat{\mathbf{u}} \quad \forall \mathbf{r} \mid z < 0, \quad (1.1)$$

where the polarization vector is

$$\begin{aligned} \hat{\mathbf{u}} = & (\cos \psi \cos \phi \cos \theta - \sin \psi \sin \phi) \hat{\mathbf{x}} + (\cos \psi \cos \phi \cos \theta + \sin \psi \cos \phi) \hat{\mathbf{y}} \\ & + \cos \psi \sin \theta \hat{\mathbf{z}}, \end{aligned} \quad (1.2)$$

and the incident wave vector is

$$\mathbf{k}_{\text{inc}} = k_{x0} \hat{\mathbf{x}} + k_{y0} \hat{\mathbf{y}} + k_{I,z00} \hat{\mathbf{z}}, \quad (1.3)$$

with

$$k_{x0} = n_1 k_0 \sin \theta \cos \phi, \quad (1.3a)$$

$$k_{y0} = n_1 k_0 \sin \theta \sin \phi, \quad (1.3b)$$

$$k_{I,z00} = n_1 k_0 \cos \theta. \quad (1.3c)$$

The free space wavenumber $k_0 = 2\pi/\lambda_0$, and the angles θ , ϕ , and ψ are defined according to convention and shown in Fig. 1.1. A time dependence of $\exp(j\omega t)$ is assumed throughout this report.

To keep the equations concise and for better numerical stability, it is advisable to keep the field magnitudes normalized so that they are of comparable magnitude. Hence, we suppose the magnetic field \mathbf{H} is normalized as

$$\mathbf{H} = -j\eta_0 \tilde{\mathbf{H}}, \quad (1.4)$$

where $\tilde{\mathbf{H}}$ is the actual, non-normalized magnetic field vector, and η_0 is the impedance of free space. We also assume that all materials are non-magnetic with a relative permeability $\mu = 1$.

The core of the RCWA approach lies in the Fourier analysis of Maxwell's curl equations, which under these constraints, simplify to

$$\nabla \times \mathbf{E} = k_0 \mathbf{H}, \quad (1.5a)$$

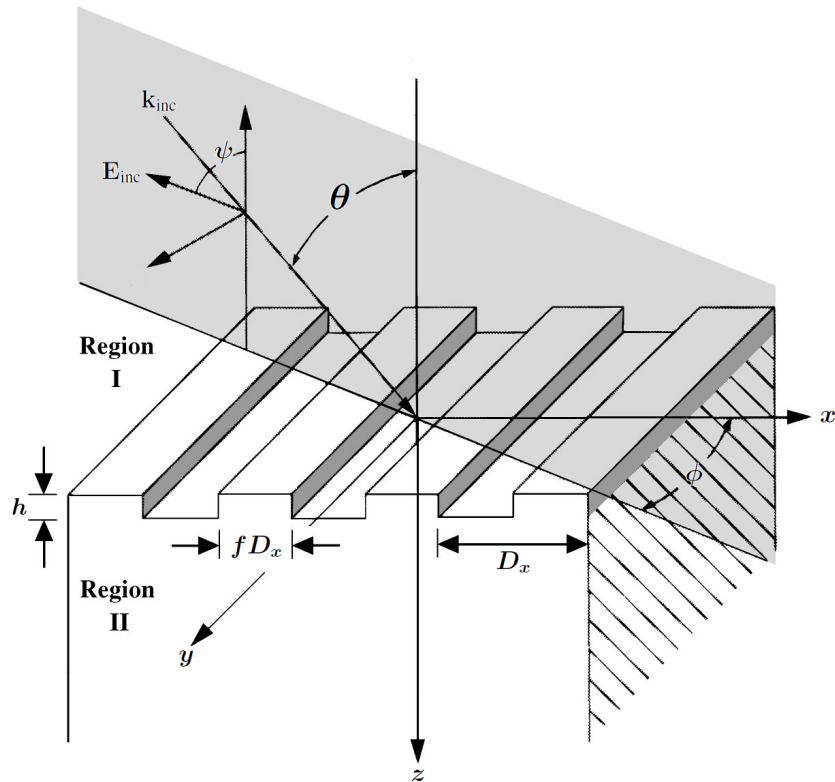


FIG. 1.1: Example of a single layered binary grating [1].

$$\nabla \times \mathbf{H} = k_0 \epsilon \mathbf{E}. \quad (1.5b)$$

We begin our analysis by calculating the Fourier series for a given permittivity distribution, which is modelled as a function $\epsilon(x, y)$ that yields the relative permittivity at (x, y) within the grating structure. The permittivity is assumed to be constant along the z -direction, but ways to relax this constraint are discussed in Chapter 3. The Fourier decomposition of this function can either be done analytically or by using the fast Fourier transform (FFT) algorithm.

The wavenumbers for the electric and magnetic fields are expanded as pseudo-periodic functions using the Floquet-Bloch theorem, which describe a wavefunction traveling across

a periodic crystal lattice [10, 11]. The fields can then be expressed as a Fourier series of mode amplitude coefficients corresponding to these wavenumbers and introduced into Maxwell's equations. The results is an eigenvalue equation for the coupling between individual components of the fields. The eigenvectors of this equation are the independent propagating modes within the grating and the eigenvalues are proportional to the propagation constants (wavenumbers) of these modes in the z -direction. The fields can be expressed using the solutions of the eigenvalue equation in terms of the (yet unknown) amplitudes for forward- and backward-traveling waves within the structure. A set of linear equations is obtained by applying the boundary conditions at region interfaces, and they are solved for these amplitude coefficients.

The series expansions of the fields and permittivity would have to be infinitely long to produce an exact solution. In practice, the series must be truncated after some finite number of terms N . Increasing the number of terms included in the calculation usually yields more accurate results, but is also more computationally demanding.

We will now consider in detail the application of this procedure to single-layered gratings.

Chapter 2

SINGLE-LAYERED GRATINGS

In this chapter, we will focus only on single-layered structures with a periodically varying electric permittivity in one direction. Single-layered structures are structures whose permittivity does not change along the direction of propagation. Moreover, the permittivity is constant in the y -direction as the direction of periodicity is assumed to be x . Hence the permittivity $\epsilon(x, y)$ is a function of x and $\epsilon(x_0 + nD_x) = \epsilon(x_0)$ for some period D_x . Thus, these structures are also referred to as 1D gratings since the permittivity only changes along a single direction.

We next review an example in which the Fourier series can be obtained analytically for a simple permittivity function.

2.1 The permittivity expansion for binary gratings

Consider again the binary 1D grating shown in figure 1.1. Let the two permittivity values be ϵ_{rd} for the “ridges” and ϵ_{gr} for the “grooves”. The permittivity function can be written as

$$\epsilon(x) = \begin{cases} \epsilon_{\text{rd}} = n_{\text{rd}}^2 & \text{if } |x| \in \left[0, \frac{fD_x}{2}\right), \\ \epsilon_{\text{gr}} = n_{\text{gr}}^2 & \text{if } |x| \in \left[\frac{fD_x}{2}, \frac{D_x}{2}\right], \end{cases} \quad (2.1)$$

where D_x is the period of the grating and the filling factor f is the fraction of the period with permittivity ϵ_{rd} .

The Fourier series expansion of $\epsilon(x)$ can be written using the Fourier transform as

$$\begin{aligned}\epsilon_m &= \frac{1}{D_x} \int_{-D_x/2}^{D_x/2} \epsilon(x) \cos(2\pi m x / D_x) dx \\ &= \frac{2}{D_x} \left[\int_0^{fD_x/2} \epsilon_{\text{rd}} \cos(2\pi m x / D_x) dx + \int_{fD_x/2}^{D_x/2} \epsilon_{\text{gr}} \cos(2\pi m x / D_x) dx \right] \\ &= (\epsilon_{\text{rd}} - \epsilon_{\text{gr}}) \frac{\sin(\pi m f)}{\pi m} = (n_{\text{rd}}^2 - n_{\text{gr}}^2) \frac{\sin(\pi m f)}{\pi m} \quad (m \neq 0),\end{aligned}\tag{2.2}$$

where m is an integer and $\epsilon_0 = n_{\text{rd}}^2 f + n_{\text{gr}}^2 (1 - f)$.

This expression is valid only for binary gratings, but it can be replaced with Fourier expansions of more complicated permittivity distributions to widen the applicability of the algorithm. Moreover, performing the FFT on a row matrix containing the permittivity values that are sampled at predefined intervals in a period yields the coefficients for any arbitrary distribution. The FFT is indispensable for most bi-periodic index profiles and is discussed in greater detail in Chapter 4. However, an analytical expression when obtainable uses less computational power and is a good starting point for the analysis of more complex structures.

2.2 TE-polarized incidence

For the grating just described, we first consider the transverse electric (TE) polarization. Here, the incident electric field is normal to the plane of incidence which is the (x, z) plane, and is polarized along the y -direction. Hence, we find that $\phi = 0$, $\psi = \pi/2$, and the incident wavevector $\mathbf{k}_{\text{inc}} = k_0(\sin \theta \hat{\mathbf{x}} + \cos \theta \hat{\mathbf{z}})$. The reflected and transmitted electric fields are expressed in terms of coefficients R_m and T_m respectively, which are to be determined.

2.2.1 Fields in the homogeneous regions

We limit our expansion of the fields to include N modes such that N is odd and $-(N-1)/2 \leq m \leq (N-1)/2$. We now write

$$E_{\text{inc},y} = \exp[-jk_0 n_I (\sin \theta x + \cos \theta z)], \quad (2.3a)$$

$$E_{\text{I},y} = E_{\text{inc},y} + \sum_m R_m \exp[-j(k_{xm}x - k_{\text{I},zm}z)], \quad (2.3b)$$

$$E_{\text{II},y} = \sum_m T_m \exp[-j(k_{xm}x + k_{\text{II},zm}(z-d))], \quad (2.3c)$$

where $E_{\text{inc},y}$ is the y -component of the incident electric field, $E_{\text{I},y}$ and $E_{\text{II},y}$ are the y -components of the electric field in the incidence and transmission regions respectively, R_m and T_m are the efficiencies of the m -th order component of the reflected and transmitted waves respectively, and the sum is carried out over the N diffraction orders.

The spatial dependence of the diffracted fields is defined in terms of the periodic wavenumbers in the x - and z -directions. The x -direction wavenumbers are expressed using the Floquet condition [11]

$$k_{xm} = n_I k_0 \sin \theta - 2\pi m / D_x, \quad (2.4)$$

while the z -direction wavenumbers are expressed using $|\mathbf{k}|^2 = (k_0 n)^2$. Thus, we find

$$k_{\rho,zm} = [(k_0 n_\rho)^2 - k_{xm}^2]^{1/2}, \quad (2.5)$$

where $\rho = \text{I, II}$ denote respectively the incidence and transmission regions. Special care must be taken to ensure that the imaginary parts of all the $k_{\rho,zm}$ are negative to prevent exponentially increasing field amplitudes, as discussed in Section 2.3.3.

The normalized magnetic field vector, \mathbf{H} from Eq. (1.4), is next expressed in the ho-

ogeneous regions in terms of the electric field. Using the reduced form of Maxwell's equation Eq. (1.5a) we obtain

$$\mathbf{H}_{\text{inc}} = V_{I,0} E_{\text{inc},y} \hat{\mathbf{x}} - K_{x0} E_{\text{inc},y} \hat{\mathbf{z}}, \quad (2.6a)$$

$$\begin{aligned} \mathbf{H}_I = \mathbf{H}_{\text{inc}} + \sum_m \left[-V_{I,m} R_m \exp[-j(k_{xm}x - k_{I,zm}z)] \hat{\mathbf{x}} \right. \\ \left. - K_{xm} R_m \exp[-j(k_{xm}x - k_{I,zm}z)] \hat{\mathbf{z}} \right], \end{aligned} \quad (2.6b)$$

$$\begin{aligned} \mathbf{H}_{II} = \sum_m \left[V_{II,m} T_m \exp[-j(k_{xm}x - k_{II,zm}(z - h))] \hat{\mathbf{x}} \right. \\ \left. - K_{xm} T_m \exp[-j(k_{xm}x - k_{II,zm}(z - h))] \hat{\mathbf{z}} \right], \end{aligned} \quad (2.6c)$$

where \mathbf{H}_{inc} is the incident magnetic field vector, \mathbf{H}_I and \mathbf{H}_{II} are the magnetic field vectors in the incidence and transmission regions respectively, and two important set of coefficients that will be used extensively are defined as

$$K_{xm} = j \frac{k_{xm}}{k_0}, \quad (2.7)$$

$$V_{\rho,m} = j \frac{k_{\rho,zm}}{k_0}. \quad (2.8)$$

2.2.2 Fields in the grating region

In the grating region ($0 < z < h$) the tangential electric and magnetic fields can be expressed as a Fourier series in terms of the spatial harmonics,

$$E_y = \sum_m E_{ym}(z) \exp(-jk_{xm}x), \quad (2.9a)$$

$$H_x = \sum_m H_{xm}(z) \exp(-jk_{xm}x). \quad (2.9b)$$

Maxwell's curl equations can also be expanded in terms of their constituent components, which for the TE-polarization reduce to

$$k_0 H_x = -\partial_z E_y, \quad (2.10a)$$

$$k_0 H_z = \partial_x E_y, \quad (2.10b)$$

$$k_0 \epsilon(x) E_y = \partial_z H_x - \partial_x H_z, \quad (2.10c)$$

where ∂_ℓ stands for a partial derivative with respect to ℓ .

Substituting (2.2) and (2.9) in Eq. (2.10) and eliminating H_z , we obtain the coupled equations,

$$\partial_z E_{ym} = -k_0 H_{xm}, \quad (2.11a)$$

$$\partial_z H_{xm} = k_0 K_{xm}^2 E_{ym} + k_0 \sum_p \epsilon_{(m-p)} E_{yp}. \quad (2.11b)$$

These equations can further be simplified by eliminating H_{xm} and on arranging the coefficients E_{ym} in a column matrix \mathbf{E}_y we obtain the differential equation

$$\partial_z^2 \mathbf{E}_y = k_0^2 (-\mathbf{K}_x^2 - \llbracket \epsilon \rrbracket) \mathbf{E}_y, \quad (2.12)$$

where $\llbracket \epsilon \rrbracket$ is the Toeplitz matrix formed by the permittivity harmonic components from Eq. (2.2) in which the (m, p) element is equal to ϵ_{m-p} . This matrix acts as a convolution operator, and \mathbf{K}_x is a diagonal matrix in which the (m, m) element is equal to K_{xm} .

2.2.3 The eigenvalue problem

Solutions to Eq. (2.12) can be obtained by making a similarity transformation of the matrix $\mathbf{A} = -\mathbf{K}_x^2 - \llbracket \epsilon \rrbracket$ so that

$$\mathbf{A} = \mathbf{W}\mathbf{\Gamma}^2\mathbf{W}^{-1}, \quad (2.13)$$

where $\mathbf{\Gamma}$ is a diagonal matrix in which the (m, m) element γ_m is equal to the square root of the m -th eigenvalue of \mathbf{A} . The columns (\mathbf{W}_n) of \mathbf{W} are the eigenvectors of \mathbf{A} . When these matrices are substituted into Eq. (2.12) we obtain a simpler differential equation

$$\partial_z^2 (\mathbf{W}^{-1}\mathbf{E}_y) = (k_0\mathbf{\Gamma})^2 (\mathbf{W}^{-1}\mathbf{E}_y). \quad (2.14)$$

As $\mathbf{\Gamma}$ is diagonal, there is no coupling among the matrix elements and the solution to Eq. (2.14) becomes

$$\mathbf{E}_y(z) = \mathbf{W} \left\{ \exp(-k_0\mathbf{\Gamma}z) \mathbf{c}^+ + \exp[k_0\mathbf{\Gamma}(z-h)] \mathbf{c}^- \right\}, \quad (2.15a)$$

which may also be written as,

$$E_{ym}(z) = \sum_n W_{m,n} \left\{ c_n^+ \exp(-k_0\gamma_n z) + c_n^- \exp[k_0\gamma_n(z-h)] \right\}, \quad (2.15b)$$

where $-(N-1)/2 \leq n \leq (N-1)/2$. The set of constants \mathbf{c}^+ and \mathbf{c}^- , are determined by the boundary conditions. The magnetic field coefficients can now be obtained from (2.11a).

Defining $\mathbf{V} = \mathbf{W}\mathbf{\Gamma}$ we obtain

$$\mathbf{H}_x(z) = \mathbf{V} \left\{ -\exp(-k_0\mathbf{\Gamma}z) \mathbf{c}^+ + \exp[k_0\mathbf{\Gamma}(z-h)] \mathbf{c}^- \right\}, \quad (2.16a)$$

$$H_{xm}(z) = \sum_{n=1}^N V_{m,n} \left\{ -c_n^+ \exp(-k_0 \gamma_n z) + c_n^- \exp[k_0 \gamma_n (z - h)] \right\}. \quad (2.16b)$$

We also define the diagonal matrices $\boldsymbol{\Phi}(z) = \exp(-k_0 \boldsymbol{\Gamma} z)$ and $\mathbf{X} = \boldsymbol{\Phi}(h)$. These matrices take into account the propagation of wave amplitudes \mathbf{c}^+ and \mathbf{c}^- . The entire z -propagation of the fields can now be written in a concise form as

$$\begin{bmatrix} \mathbf{E}_y(z) \\ \mathbf{H}_x(z) \end{bmatrix} = \begin{bmatrix} \mathbf{W} & \mathbf{W} \\ \mathbf{V} & -\mathbf{V} \end{bmatrix} \begin{bmatrix} \boldsymbol{\Phi}(z) & \mathbf{0} \\ \mathbf{0} & \mathbf{X}\boldsymbol{\Phi}(-z) \end{bmatrix} \begin{bmatrix} \mathbf{c}^+ \\ \mathbf{c}^- \end{bmatrix}. \quad (2.17)$$

The eigenvalues γ_n govern the phase change along the z -direction of the fields, including their attenuation or gain. They are equivalent to the z -direction wavenumber in the incidence and transmission regions $k_{\rho,zn}$. Thus, for the homogeneous regions we see that $\gamma_{\rho,n} = j(k_{\rho,zn}/k_0)$, and we can use this observation to define $\boldsymbol{\Gamma}_\rho$ and $\boldsymbol{\Phi}_\rho(z)$.

The unknown constants c_n^+ and c_n^- , are the amplitudes of the n th eigenmode for the forward- and backward-propagating waves respectively. They are equivalent to T_m and R_m defined in Eq. (2.3). The incident wave is assumed monochromatic and hence its amplitude coefficient matrix is the Kronecker delta column matrix $\boldsymbol{\delta}_0$ which is 1 only for index $m = 0$ and 0 elsewhere.

The n -th column of the eigenvector matrices \mathbf{W} and \mathbf{V} equals the relative intensity of the individual field harmonics that make up the eigenmodes of the grating structure. It follows that \mathbf{W}_n and \mathbf{V}_n are the standard basis vectors of the structure for the electric and magnetic fields respectively, and these components will travel unperturbed through the medium. The homogeneous counterpart of these matrices may not seem obvious from Eq. (2.3). Hence, using Eq. (2.6), our recent definition of $\gamma_{\rho,n}$, and defining \mathbf{V}_ρ as a diagonal matrix with $\gamma_{\rho,m}$ as its (m, m) element, we can use the definition for \mathbf{V} , from which we find that $\mathbf{W}_\rho = \mathbf{I}$, where \mathbf{I} is an $N \times N$ identity matrix.

Using this insight we can express the electric and magnetic fields in the homogeneous regions in a matrix equation similar to (2.17) as

$$\begin{bmatrix} \mathbf{E}_{I,y}(z) \\ \mathbf{H}_{I,x}(z) \end{bmatrix} = \begin{bmatrix} \mathbf{W}_I & \mathbf{W}_I \\ \mathbf{V}_I & -\mathbf{V}_I \end{bmatrix} \begin{bmatrix} \Phi_I(z) & \mathbf{0} \\ \mathbf{0} & \Phi_I(-z) \end{bmatrix} \begin{bmatrix} \delta_0 \\ \mathbf{R} \end{bmatrix}, \quad (2.18a)$$

$$\begin{bmatrix} \mathbf{E}_{II,y}(z) \\ \mathbf{H}_{II,x}(z) \end{bmatrix} = \begin{bmatrix} \mathbf{W}_{II} & \mathbf{W}_{II} \\ \mathbf{V}_{II} & -\mathbf{V}_{II} \end{bmatrix} \begin{bmatrix} \Phi_{II}(z-h) & \mathbf{0} \\ \mathbf{0} & \Phi_{II}(h-z) \end{bmatrix} \begin{bmatrix} \mathbf{T} \\ \mathbf{0} \end{bmatrix}. \quad (2.18b)$$

2.2.4 Boundary conditions

Equations 2.17 and 2.18 form the backbone of the approach that we will apply to multilayer gratings in Chapter 3. Among these equations we have 4 unknown matrices \mathbf{R} , \mathbf{T} , \mathbf{c}^+ , and \mathbf{c}^- . To find them, we apply the boundary conditions by matching the tangential components of the fields at $z = 0$ and $z = h$, which yields

$$\begin{bmatrix} \mathbf{I} & \mathbf{I} \\ \mathbf{V}_I & -\mathbf{V}_I \end{bmatrix} \begin{bmatrix} \delta_0 \\ \mathbf{R} \end{bmatrix} = \begin{bmatrix} \mathbf{W} & \mathbf{W}\mathbf{X} \\ \mathbf{V} & -\mathbf{V}\mathbf{X} \end{bmatrix} \begin{bmatrix} \mathbf{c}^+ \\ \mathbf{c}^- \end{bmatrix}, \quad (2.19a)$$

$$\begin{bmatrix} \mathbf{I} & \mathbf{I} \\ \mathbf{V}_{II} & -\mathbf{V}_{II} \end{bmatrix} \begin{bmatrix} \mathbf{T} \\ \mathbf{0} \end{bmatrix} = \begin{bmatrix} \mathbf{W}\mathbf{X} & \mathbf{W} \\ \mathbf{V}\mathbf{X} & -\mathbf{V} \end{bmatrix} \begin{bmatrix} \mathbf{c}^+ \\ \mathbf{c}^- \end{bmatrix}. \quad (2.19b)$$

Since each of the matrix equation is in fact a pair of equations we may eliminate \mathbf{R} from Eqs. (2.19a) and \mathbf{T} from Eqs. (2.19b) and concatenate them in a single matrix equation to obtain

$$\begin{bmatrix} 2\mathbf{V}_I\delta_0 \\ \mathbf{0} \end{bmatrix} = \begin{bmatrix} \mathbf{W}\mathbf{V}_I + \mathbf{V} & (\mathbf{W}\mathbf{V}_I - \mathbf{V})\mathbf{X} \\ (\mathbf{W}\mathbf{V}_{II} - \mathbf{V})\mathbf{X} & \mathbf{W}\mathbf{V}_{II} + \mathbf{V} \end{bmatrix} \begin{bmatrix} \mathbf{c}^+ \\ \mathbf{c}^- \end{bmatrix}. \quad (2.20)$$

We use this expression to solve for $\mathbf{C} = \begin{bmatrix} \mathbf{c}^+ & \mathbf{c}^- \end{bmatrix}^T$ where T stands for the transpose. Substituting \mathbf{C} into (2.19), we obtain \mathbf{R} and \mathbf{T} as

$$\begin{bmatrix} \mathbf{I} \\ -\mathbf{V}_I \end{bmatrix} \mathbf{R} = \begin{bmatrix} \mathbf{W} & \mathbf{WX} \\ \mathbf{V} & -\mathbf{VX} \end{bmatrix} \begin{bmatrix} \mathbf{c}^+ \\ \mathbf{c}^- \end{bmatrix} - \begin{bmatrix} \mathbf{I} \\ -\mathbf{V}_I \end{bmatrix} \delta_0, \quad (2.21a)$$

$$\begin{bmatrix} \mathbf{I} \\ \mathbf{V}_{II} \end{bmatrix} \mathbf{T} = \begin{bmatrix} \mathbf{WX} & \mathbf{W} \\ \mathbf{VX} & -\mathbf{V} \end{bmatrix} \begin{bmatrix} \mathbf{c}^+ \\ \mathbf{c}^- \end{bmatrix}. \quad (2.21b)$$

Finally, the reflected and transmitted diffraction efficiencies of the m -th order component, DE_{rm} and DE_{tm} respectively, can be calculated using

$$DE_{rm} = |R_m|^2 \operatorname{Re} \left(\frac{\gamma_{I,m}}{\gamma_{I,0}} \right), \quad (2.22a)$$

$$DE_{tm} = |T_m|^2 \operatorname{Re} \left(\frac{\gamma_{II,m}}{\gamma_{II,0}} \right). \quad (2.22b)$$

where $\operatorname{Re}(x)$ denotes the real part of x .

2.2.5 Estimating the fields

Once we find the amplitude coefficients, we have calculated the behaviour of the light that is incident on the grating structure. The transverse components of the fields have already been expressed in Eq. (2.17). Including the lateral component \mathbf{H}_z , we obtain

$$\begin{bmatrix} \mathbf{E}_y(z) \\ \mathbf{H}_x(z) \\ \mathbf{H}_z(z) \end{bmatrix} = \begin{bmatrix} \mathbf{W} & \mathbf{W} \\ \mathbf{V} & -\mathbf{V} \\ -\mathbf{V}_z & -\mathbf{V}_z \end{bmatrix} \begin{bmatrix} \Phi(z) & \mathbf{0} \\ \mathbf{0} & \mathbf{X}\Phi(-z) \end{bmatrix} \begin{bmatrix} \mathbf{c}^+ \\ \mathbf{c}^- \end{bmatrix}. \quad (2.23)$$

We make use of $k_0 H_z = \partial_x E_y$ to obtain $\mathbf{H}_z = -\mathbf{K}_x \mathbf{E}_y$, which implies that

$$\mathbf{V}_z = \mathbf{K}_x \mathbf{W}. \quad (2.24)$$

As we have the same equation describing the z -propagation of the fields in all regions, we can generalize this result. We denote the first matrix on the right hand-side of Eq. (2.23) containing the eigenvector matrices (\mathbf{W} , \mathbf{V} , \mathbf{V}_z) as \mathbf{M} . The matrix \mathbf{M} contains the mode coupling information. We denote the second matrix on the right hand-side of Eq. (2.23) as $\Phi(z)$. We now find

$$\Psi_\rho(z) = \mathbf{M}_\rho \Phi_\rho(z) \mathbf{C}_\rho, \quad (2.25)$$

where $\Psi_\rho = \begin{bmatrix} \mathbf{E}_y(z) & \mathbf{H}_x(z) & \mathbf{H}_z(z) \end{bmatrix}^T$ is the matrix containing all non-zero components of the fields in region ρ . Multiplying each of those components with $\Phi_x(x) = \exp(-k_0 \mathbf{K}_x x)$ yields the complex magnitude of that field component at any point in the (x, z) plane. Thus, by defining

$$\Phi_x(x) = \begin{bmatrix} \Phi_x(x) & \mathbf{0} & \mathbf{0} \\ \mathbf{0} & \Phi_x(x) & \mathbf{0} \\ \mathbf{0} & \mathbf{0} & \Phi_x(x) \end{bmatrix}, \quad (2.26)$$

we can obtain the fields diffracted from a single layer of gratings with the equation

$$\Psi_\rho(x, z) = \Phi_x(x) \mathbf{M}_\rho \Phi_\rho(z) \mathbf{C}_\rho. \quad (2.27)$$

2.2.6 Chalcogenide glass

To test this portion of the algorithm, we consider the structure studied in [6]. The authors discuss the asymmetric resonances caused by subwavelength slits in a single layer of As_2S_3 etched on glass ($n_{\text{II}} = 1.52$), as shown in Fig. 2.1a. An implementation in MATLAB based on the equations in Section 2.2 was able to accurately recreate the expected response and the results are displayed in Fig. 2.1b.

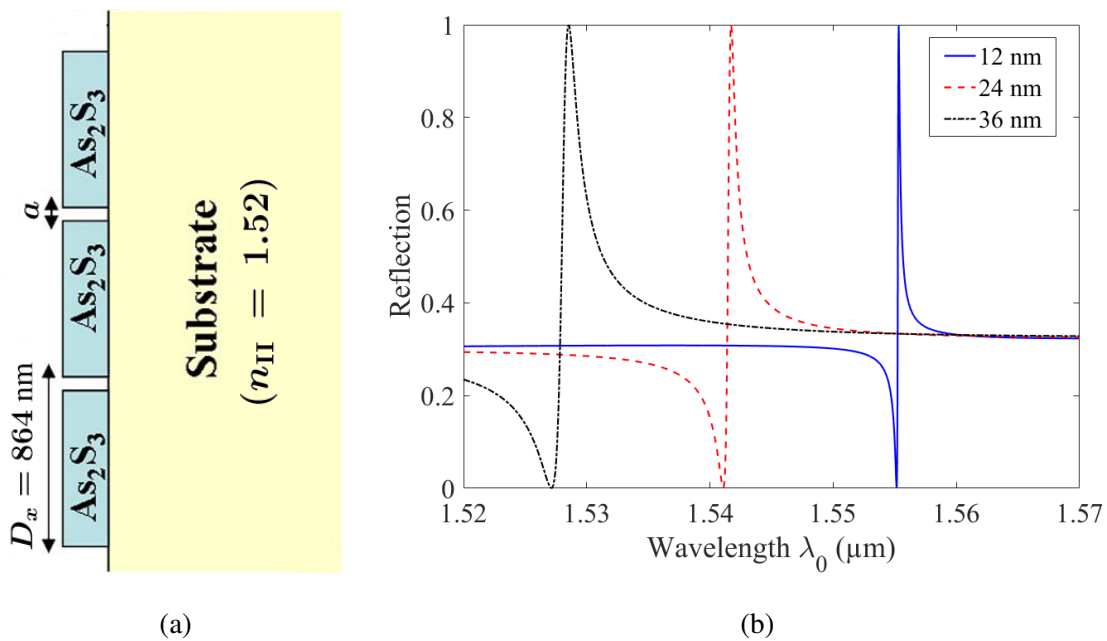


FIG. 2.1: **(a)** The basic structure of the As_2S_3 grating used to test the algorithm for 1D gratings [6]. Thickness $h = 200$ nm. **(b)** Reflection resonances for three slit sizes of chalcogenide glass a .

2.3 TM Polarization

It was found that when the approach we described for TE-polarized light is repeated for transverse-magnetic (TM) polarized light, the convergence obtained by increasing the number of harmonics is slow. Hence, corrections have been introduced in the algorithm [12, 13]. Before proceeding to the corrections, let us follow the same procedure as before for TM-polarized incidence and discuss why these corrections appear.

2.3.1 The classical approach

Instead of starting with the equations of the electric field, as we did in Section 2.2, we start out with equations for the magnetic field. Thus, we write

$$H_{\text{inc},y} = \exp[-jk_0 n_1 (\sin \theta x + \cos \theta z)], \quad (2.28a)$$

$$H_{\text{I},y} = H_{\text{inc},y} + \sum_m R_m \exp[-j(k_{xm}x - k_{\text{I},zm}z)], \quad (2.28b)$$

$$H_{\text{II},y} = \sum_m T_m \exp[-j(k_{xm}x + k_{\text{II},zm}(z - d))]. \quad (2.28c)$$

where $H_{\text{inc},y}$ is the y -component of the incident magnetic field, while $H_{\text{I},y}$ and $H_{\text{II},y}$ are the y -components of the magnetic field in the incidence and transmission regions respectively.

By using Eq. (1.5b) we obtain the following expressions for the electric field,

$$\mathbf{E}_{\text{inc}} = V_{\text{I},0} E_{\text{inc},y} \hat{\mathbf{x}} - K_{\text{I},x0} E_{\text{inc},y} \hat{\mathbf{z}}, \quad (2.29a)$$

$$\begin{aligned} \mathbf{E}_{\text{I}} = \mathbf{E}_{\text{inc}} + \sum_m \left[-V_{\text{I},m} R_m \exp[-j(k_{xm}x - k_{\text{I},zm}z)] \hat{\mathbf{x}} \right. \\ \left. - K_{xm} R_m \exp[-j(k_{xm}x - k_{\text{I},zm}z)] \hat{\mathbf{z}} \right], \end{aligned} \quad (2.29b)$$

$$\begin{aligned} \mathbf{E}_{\text{II}} = \sum_m \left[V_{\text{I},m} T_m \exp[-j(k_{xm}x - k_{\text{II},zm}(z - h))] \hat{\mathbf{x}} \right. \\ \left. - K_{\text{II},xm} T_m \exp[-j(k_{xm}x - k_{\text{II},zm}(z - h))] \hat{\mathbf{z}} \right]. \end{aligned} \quad (2.29c)$$

where \mathbf{E}_{inc} is the incident electric field vector, \mathbf{E}_{I} and \mathbf{E}_{II} are the electric field vectors in the incidence and transmission regions respectively. The equations appear similar to Eq. (2.6), but we note that \mathbf{V} now acts on the magnetic field to yield the electric field instead of vice versa. The appearance of the relative permittivity n_ρ^2 in the Maxwell's equation used here changes the definitions of K_{xm} and $V_{\rho,m}$. So, for the TM-polarization, we find

$$K_{\rho,xm} = j \frac{k_{xm}}{n_\rho^2 k_0}, \quad V_{\rho,m} = j \frac{k_{\rho,zm}}{n_\rho^2 k_0}. \quad (2.30)$$

The Fourier expansions of the fields in the region $0 < z < h$ becomes

$$H_y = \sum_m H_{ym}(z) \exp(-jk_{xm}x), \quad (2.31a)$$

$$E_x = \sum_m E_{xm}(z) \exp(-jk_{xm}x). \quad (2.31b)$$

Analogous to how we obtained Eqs. (2.10), we solve Maxwell's equations for their individual components and eliminate E_z to obtain the coupled equations

$$k_0 \epsilon E_x = -\partial_z H_y, \quad (2.32a)$$

$$k_0 H_y = \partial_z E_x - \partial_x \left(\frac{1}{\epsilon} \partial_x H_y \right). \quad (2.32b)$$

At first glance, these equations seem very similar to the ones in (2.10), and we could continue to follow the same steps that we described previously and arrive at

$$\partial_z \mathbf{H}_y = -k_0 \llbracket \epsilon \rrbracket \mathbf{E}_x, \quad (2.33a)$$

$$\partial_z \mathbf{E}_x = k_0 \mathbf{H}_y + k_0 \mathbf{K}_x \llbracket \frac{1}{\epsilon} \rrbracket \mathbf{K}_x \mathbf{H}_y. \quad (2.33b)$$

Note that the matrix $\llbracket 1/\epsilon \rrbracket$ is not the same as $1/\llbracket \epsilon \rrbracket$. This matrix has as its elements the

Fourier coefficients of the inverse permittivity function $\zeta(x) = [\epsilon(x)]^{-1}$. For the uniperiodic binary grating described in Fig. 1.1 we have,

$$\zeta_0 = n_{\text{rd}}^{-2}f + n_{\text{gr}}^{-2}(1 - f), \quad \zeta_m = (n_{\text{rd}}^{-2} - n_{\text{gr}}^{-2}) \frac{\sin(\pi m f)}{\pi m}. \quad (2.34)$$

The (m, n) element of the Toeplitz matrix $[[1/\epsilon]]$ is equal to ζ_{m-n} . This matrix will henceforth be referred to as $[[\zeta]]$.

It is possible to proceed by formulating an eigenvalue problem using Eq. (2.33), but the rate of convergence as N increases, where N is number of Fourier modes that are included in the field expansion, is poor compared to the TE-polarized case [12, Fig. 2]. The solution to this problem was suggested by Lalanne and Morris [12] in 1996, and the mathematical reasoning behind it was presented by Li [13].

2.3.2 An improved formulation for the TM-polarization

Consider a function $h(x)$ such that $h(x) = f(x)g(x)$ where f and g are piecewise continuous functions having the same period. Li outlines three rules that suggest how one might best transform this spatial relationship into the frequency domain, *i.e.* express the harmonic amplitude coefficients h_m of $h(x)$ in terms of f_m and g_m .

Rule 1. If f and g do not share any points of discontinuity, then $h(x)$ should be transformed using the Laurent rule:

$$h_m^{(N)} = \sum_{m=-N}^N f_{m-n} g_n, \quad \text{or} \quad \mathbf{h}^{(N)} = [[f]] \mathbf{g}. \quad (2.35)$$

We effectively made use of this relation in Eq. (2.11b) as there are no concurrent discontinuities between ϵ and E_y .

Rule 2. If the concurrent discontinuities in f and g are such that their product h is still

continuous, then they are pairwise complimentary discontinuities. The Laurent rule is no longer the best approach. The situation can still be easily rectified. If $f(x)$ is invertible, then for

$$g(x) = \frac{1}{f(x)}h(x)$$

rule 1 holds. This relation can now be written in terms of the harmonic coefficients as

$$\sum_m \left(\frac{1}{f}\right)_{m-n} h_m^{(N)} = g_n, \quad \text{or} \quad \mathbf{h}^{(N)} = \left[\left[\frac{1}{f}\right]\right]^{-1} \mathbf{g}. \quad (2.36)$$

This rule will be called the inverse rule.

Rule 3. A product of two functions having concurrent, but not complimentary discontinuities cannot be transformed accurately by the rules described above. Such products are to be avoided.

Equipped with this new information, let us re-analyze Eq. (2.32). Maxwell's equations tell us that the product ϵE_x is continuous across the regions of different permittivity since E_x is the component of electric field normal to changes in ϵ . We know that ϵ is discontinuous, so E_x and ϵ must have pairwise complimentary discontinuities. Hence, this product should be transformed according to the inverse rule, and Eq. (2.32a) yields

$$\partial_z \mathbf{H}_y = -k_0 \llbracket \zeta \rrbracket^{-1} \mathbf{E}_x. \quad (2.37a)$$

For Eq. (2.32b), the product $[(1/\epsilon)\partial_x H_y]$ is of interest. Once again, the physics tells us that this product should be transformed using the inverse rule.

$$\partial_z \mathbf{H}_x = k_0 \mathbf{E}_y + k_0 \mathbf{K}_x \llbracket \epsilon \rrbracket^{-1} \mathbf{K}_x \mathbf{H}_y. \quad (2.37b)$$

The equations are now in a numerically stable form. We eliminate \mathbf{E}_x to find the eigenvalue equation for the magnetic field modes

$$\partial_z^2 \mathbf{H}_y = -k_0^2 \llbracket \zeta \rrbracket^{-1} (\mathbf{I} + \mathbf{K}_x \llbracket \epsilon \rrbracket^{-1} \mathbf{K}_x) \mathbf{H}_y. \quad (2.38)$$

To solve this eigenvalue equation, we define $\mathbf{A} = -\llbracket \zeta \rrbracket^{-1} (\mathbf{I} + \mathbf{K}_x \llbracket \epsilon \rrbracket^{-1} \mathbf{K}_x)$ and proceed as in Section 2.2.3. However, the matrix \mathbf{W} in this case, computes the amplitude coefficients for the magnetic field. So, to compute \mathbf{V} we must use Eq. (2.37a). Hence for the TM-polarization, we find

$$\mathbf{V} = \llbracket \zeta \rrbracket \mathbf{W} \boldsymbol{\Gamma}. \quad (2.39)$$

2.3.3 Dealing with a complex permittivity: Diffraction in silver gratings

In order to test the TM formulation we refer to [7], which describes diffraction through metallic gratings with narrow slits. The relative permittivity of the silver, the grating material in question here, is a complex number. The dispersion of Ag is discussed by Palik [14].

If we simply write $\epsilon_{\text{rd}} = \text{Re}(\epsilon_{\text{Ag}}) + j \text{Im}(\epsilon_{\text{Ag}})$, the results are unphysical. We note that the operator $\text{Im}(x)$ stands for the imaginary part of (x) . We assumed a convention that $\exp(-j\epsilon k_z z)$ indicates a propagation in positive z -direction, and we also assumed that loss in a medium is characterized by a negative value for the imaginary part of the permittivity. Thus, we find that if $\text{Im}(\epsilon_{\text{Ag}})$ is positive the z -propagation term now includes an increasing exponential term $\exp[\text{Im}(\epsilon) k_z z]$ which results in a violation of conservation in energy. Instead, we demand that $\epsilon_{\text{rd}} = \text{Re}(\epsilon_{\text{Ag}}) - j \text{Im}(\epsilon_{\text{Ag}})$.

Fig. 2.2b shows the transmission of the gratings described in Fig. 2.2a and is in agreement with Fig. 3 from [7].

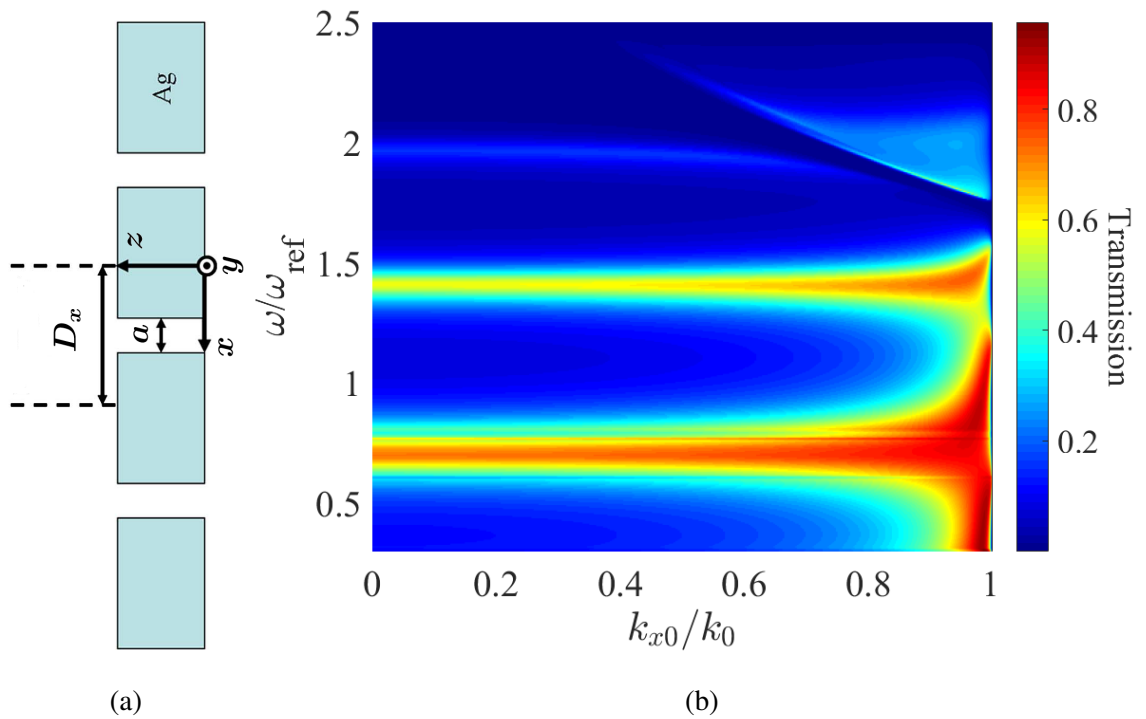


FIG. 2.2: **(a)** D’Aguanno et al. [7, Fig. 1]. The basic geometry of the silver gratings. For this example, we set $D_x = 285$ nm, $a = 32$ nm, and $h = 400$ nm. **(b)** Transmission spectrum of the gratings where $\omega/\omega_{\text{ref}} = 1/\lambda_0$.

Chapter 3

MULTIPLE LAYERS

Now that the techniques to model the fields and diffraction for the case of single-layer gratings have been discussed, we proceed to a more complex situation. In this chapter, we will consider the techniques that can be applied to structures in which the permittivity distribution function $\epsilon(x, y)$ may change along the direction of propagation z . Since the permittivity can now vary along two directions, these are also called 2D structures. It is not practical to solve Maxwell's equations for such a situation by considering the entire structure to be a single layer. However, if the structure can be broken down into finitely many single-layer gratings having the same period, then the ideas presented in the previous section can be extended to find the solutions.

3.1 Lamellarization

The first step is to approximate the structure in such a way that the theory developed in the previous section can be used. For the case of binary gratings, we define two piecewise constant functions $f(z)$ and $h(z)$ in $0 < z < h$ such that

$$h(z) = h_l \quad \text{and} \quad f(z) = f_l, \quad (3.1)$$

for $z_{l-1} < z < z_l$, where $z_l = \sum_{i=1}^l h_i$ is the z -coordinate for the end of layer l . Furthermore, if the total number of layers is L , then we define $h_1 = f_1 = 0$ for the incidence layer and $h_L = f_L = 0$ for the transmission layer. Note that the regions I and II are renumbered as 1 and L for consistency. In this notation, the gratings discussed in the previous section had $L = 3$ with $h_2 = h$ and $f_2 = f$. For structures that do not have an analytical Fourier series, we can build a matrix where the elements in each row are the permittivity values of a layer sampled at predefined intervals and use the FFT to obtain the Fourier series of the permittivity for each layer.

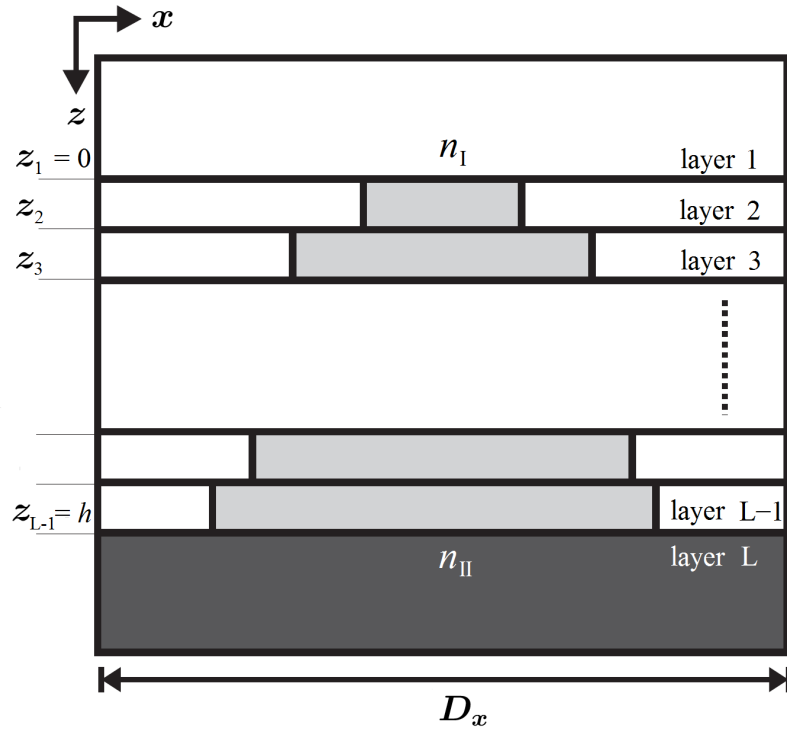


FIG. 3.1: The decomposition of a 2D structure into many thin layers [8].

Once we obtain these Fourier coefficients we can build the permittivity Toeplitz matrices $[[\epsilon]]$. The eigenvalue equation, which is Eq. (2.12) for TE-polarized waves and Eq. (2.38) for TM-polarized waves, is then solved independently for each layer. Finally we apply the

boundary conditions at every interface.

Here, the 2D formulation requires a novel approach. As we may have an arbitrary number of linear equations, traditional techniques to solve them are computationally inefficient. We now describe two common approaches to solve a large set of linear equations.

3.2 Calculating the efficiencies: The S-matrix method

The first approach eliminates two out of the four unknown sets of coefficients from each interface equation. We then obtain an equation in terms of \mathbf{R} , \mathbf{T} , and the incident wave coefficients, which we have already assumed to equal δ_0 . From among many iterative methods, one of the most efficient has been shown to be the S-matrix, or scattering matrix method [2]. It was

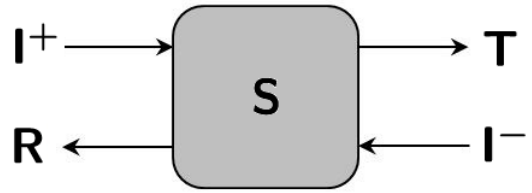


FIG. 3.2: Schematic representation of the S-matrix as a four-port system.

developed for experiments in high energy physics, where the probability outcomes of various scattering processes are of interest. Here we will formulate a method that utilizes the properties of scattering matrices to solve the boundary conditions arising from Maxwell's equations.

Consider a system with two inputs and two outputs as shown in Fig. 3.2. The S-matrix for this system defines a linear relation between the outputs and inputs. In quantum mechanics, it is used as an operator that when applied to the incoming wavefunction computes the outgoing waves,

$$\Psi_{\text{out}} = \hat{\mathbf{S}}\Psi_{\text{in}}. \quad (3.2)$$

where Ψ_{in} and Ψ_{out} are the incoming and outgoing waves respectively and $\hat{\mathbf{S}}$ is the S-matrix

operator.

For the situation of interest here, we find

$$\begin{bmatrix} \mathbf{T} \\ \mathbf{R} \end{bmatrix} = \mathbf{S} \begin{bmatrix} \mathbf{I}^+ \\ \mathbf{I}^- \end{bmatrix}, \quad (3.3)$$

where \mathbf{I}^+ is the wave incident from region 1, and \mathbf{I}^- is the wave incident from region L .

The matrix \mathbf{S} can be decomposed as

$$\mathbf{S} = \begin{bmatrix} \mathbf{S}_{uu} & \mathbf{S}_{ud} \\ \mathbf{S}_{du} & \mathbf{S}_{dd} \end{bmatrix}, \quad (3.4)$$

from which we obtain

$$\mathbf{T} = \mathbf{S}_{uu}\mathbf{I}^+ + \mathbf{S}_{ud}\mathbf{I}^-, \quad (3.5a)$$

$$\mathbf{R} = \mathbf{S}_{du}\mathbf{I}^+ + \mathbf{S}_{dd}\mathbf{I}^-. \quad (3.5b)$$

The real utility of the S-matrix however, lies in consolidating many systems into a single system. Fig. 3.3 shows a situation where two such systems are stacked. One of the outputs of system \mathbf{S}_1 , \mathbf{c}^+ , acts as an input to the next system \mathbf{S}_2 and one output from \mathbf{S}_2 , \mathbf{c}^- , acts as input to \mathbf{S}_1 . Thus we can have no information about \mathbf{c}^- unless we apply \mathbf{S}_2 to its inputs, for which we need to know \mathbf{c}^+ . Such situations can be simplified using the combination property of the S matrix, sometimes referred to as the Redheffer star product. A linear relation can be algebraically worked out between the final inputs and outputs using equations (3.5a) for both \mathbf{S}_1 and \mathbf{S}_2 . Eliminating \mathbf{c}^+ and \mathbf{c}^- , we find that the relation

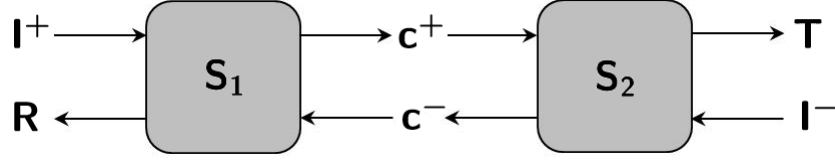


FIG. 3.3: Stacking of two systems represented as S-matrices.

between I^+ , I^- , R and T can be expressed using a single S-matrix S , which consists of

$$\begin{aligned}
 S_{uu} &= S_{2uu} (\mathbf{I} - S_{1ud} S_{2du})^{-1} S_{1uu} , \\
 S_{ud} &= S_{2ud} + S_{2uu} S_{1ud} (\mathbf{I} - S_{2du} S_{1ud})^{-1} S_{2dd} , \\
 S_{du} &= S_{1du} + S_{1dd} S_{2du} (\mathbf{I} - S_{1ud} S_{2du})^{-1} S_{1uu} , \\
 S_{dd} &= S_{1dd} (\mathbf{I} - S_{2du} S_{1ud})^{-1} S_{2dd} .
 \end{aligned} \tag{3.6}$$

This relationship is usually denoted $S = S_1 \star S_2$.

3.2.1 Implementing the S matrix for single-layered gratings

As a simple example of the S-matrix formulation, we will re-examine the single-layered gratings. The systems S_1 and S_2 now correspond to the incidence and transmission interfaces. We rearrange the terms to obtain a matrix that relates the incoming wave amplitudes to the outgoing amplitudes. Eq. (2.19a) may be written as

$$\begin{bmatrix} c^+ \\ R \end{bmatrix} = \begin{bmatrix} W_2 & -I \\ V_2 & V_1 \end{bmatrix}^{-1} \begin{bmatrix} I & -W_2 X \\ V_1 & V_2 X \end{bmatrix} \begin{bmatrix} I^+ \\ c^- \end{bmatrix} , \tag{3.7}$$

which has the form of an S-matrix with

$$\mathbf{S}_1 = \begin{bmatrix} \mathbf{W}_2 & -\mathbf{I} \\ \mathbf{V}_2 & \mathbf{V}_1 \end{bmatrix}^{-1} \begin{bmatrix} \mathbf{I} & -\mathbf{W}_2\mathbf{X} \\ \mathbf{V}_1 & \mathbf{V}_2\mathbf{X} \end{bmatrix}. \quad (3.8)$$

Similarly, from Eq. (2.19b) we obtain

$$\mathbf{S}_2 = \begin{bmatrix} \mathbf{I} & -\mathbf{W}_2 \\ \mathbf{V}_3 & \mathbf{V}_2 \end{bmatrix}^{-1} \begin{bmatrix} \mathbf{W}_2\mathbf{X} & -\mathbf{I} \\ \mathbf{V}_2\mathbf{X} & \mathbf{V}_2 \end{bmatrix}. \quad (3.9)$$

The coefficients for \mathbf{S}_1 and \mathbf{S}_2 stand for the index of the interface between layers. Taking the star product, we obtain the final S-matrix that accurately models the diffraction produced by the grating, due to incident waves from either direction.

3.2.2 A generalized approach

Recall $\mathbf{W} = \mathbf{I}$ and also that $\mathbf{X} = \mathbf{I}$ for the incidence and transmission layers. Thus, we may express the S-matrix for any interface ℓ as

$$\mathbf{S}_\ell = \begin{bmatrix} \mathbf{W}_{\ell+1} & -\mathbf{W}_\ell \\ \mathbf{V}_{\ell+1} & \mathbf{V}_\ell \end{bmatrix}^{-1} \begin{bmatrix} \mathbf{W}_\ell\mathbf{X}_\ell & -\mathbf{W}_{\ell+1}\mathbf{X}_{\ell+1} \\ \mathbf{V}_\ell\mathbf{X}_\ell & \mathbf{V}_{\ell+1}\mathbf{X}_{\ell+1} \end{bmatrix}. \quad (3.10)$$

In the case of a single layer, we only had three layers and two interfaces, but in Section 3.1 we showed how a grating can be decomposed into any number of interfaces. Hence, we take the star product of S-matrices for all the interfaces, which number $L - 1$ for L layers,

$$\mathbf{S} = \mathbf{S}_1 \star \mathbf{S}_2 \star \cdots \star \mathbf{S}_{L-1}. \quad (3.11)$$

Once we obtain this final S matrix, the transmitted and reflected wave amplitudes can be

obtained from Eq. (3.3). For unit-amplitude monochromatic incidence from a single direction, we have

$$\mathbf{T} = \mathbf{S}_{\text{uu}} \boldsymbol{\delta}_0, \quad \text{and} \quad \mathbf{R} = \mathbf{S}_{\text{du}} \boldsymbol{\delta}_0. \quad (3.12)$$

3.2.3 Results

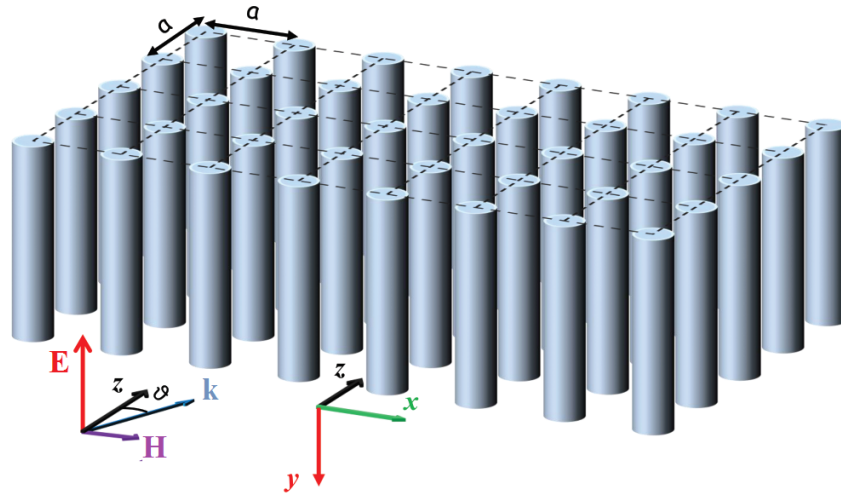
The S-matrix implementation was tested using the photonic structures shown in Fig. 3.4 from [9]. The results shown in Figs. 3.5 and 3.6 for TE- and TM-polarized incidence respectively, show a sharp drop in transmission at a very small incidence angle. The frequency at this resonance is called the Dirac point, and it is in agreement with [9].

3.3 Fields within the structure: The big matrix approach

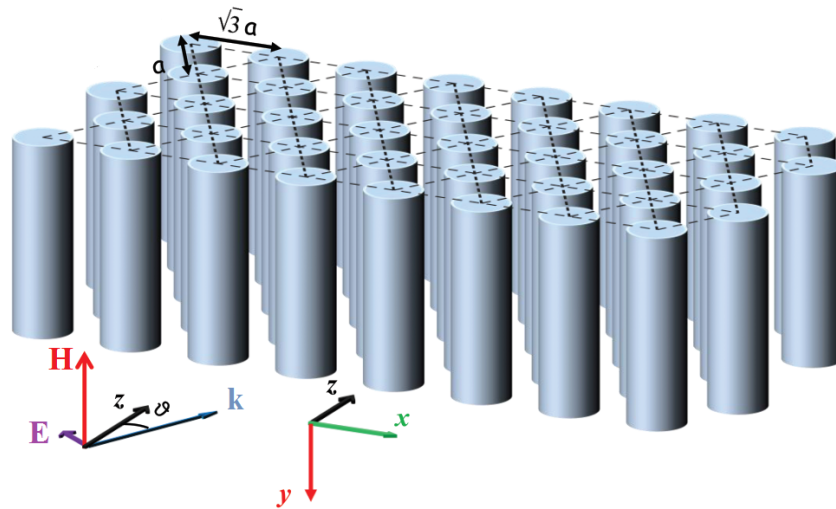
Since the amplitude coefficients of the internal layers are eliminated, the S-matrix method does not facilitate the process of obtaining the fields inside the structure. To calculate these fields, we need an equation that expresses the amplitude coefficients of a layer in terms of the coefficients of an adjacent layer, which can be done by converting the S-matrix into a transmission or T-matrix, which appears in the relation

$$\mathbf{C}_\rho = \mathbf{TC}_{\rho-1}. \quad (3.13)$$

However, the transmission matrix includes exponentially diverging products of $\Phi(z)$ and is numerically unstable. This inability of the S-matrix to resolve the fields inside the structure arises because it is calculated recursively. Each star product in the formulation is equivalent to adding a single layer. The impact of the fields in the remaining layers is then adjusting in the later products. This step-by-step approach can be avoided by building a large matrix containing the eigenvector matrices of all the layers so that when it is applied



(a)



(b)

FIG. 3.4: **(a)** D’Aguanno et al. [9, Fig. 1a]. Structure for the results shown in Figs. 3.5 with the following parameters: number of rows $N_r = 5$, $r/a = 0.2$, $a = 1 \mu\text{m}$, and relative permittivity of columns $\epsilon = 12.5$. **(b)** Structure for the plots in Figs. 3.6. Correctly labelled version of [9, Fig. 7a] with parameters: $N_r = 5$, $r/a = 0.2$, $\epsilon = 11.4$.

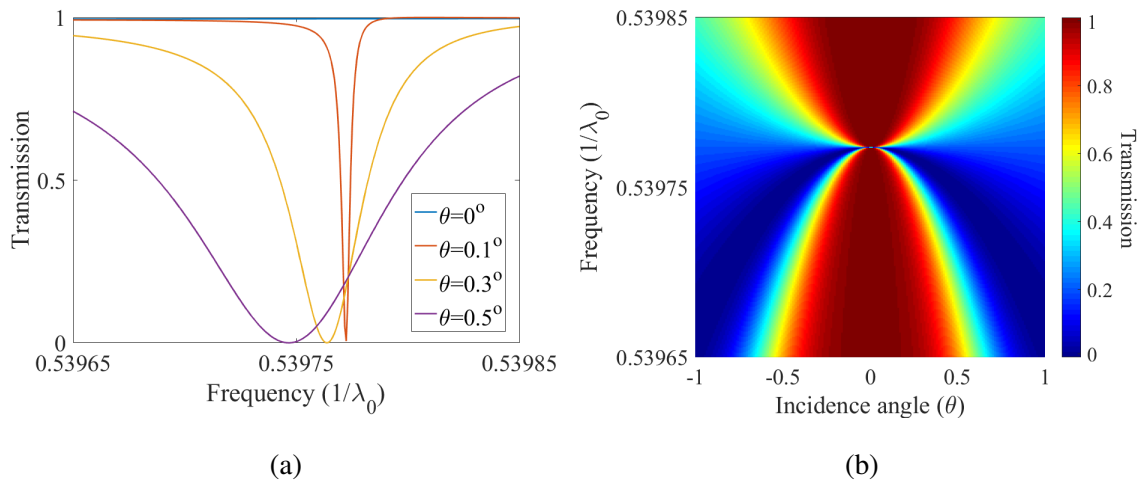


FIG. 3.5: Transmission spectrum for TE-polarized incidence on 2D gratings shown in Fig. 3.4a. Reproduction of (a) [9, Fig. 2] and (b) [9, Fig. 1b].

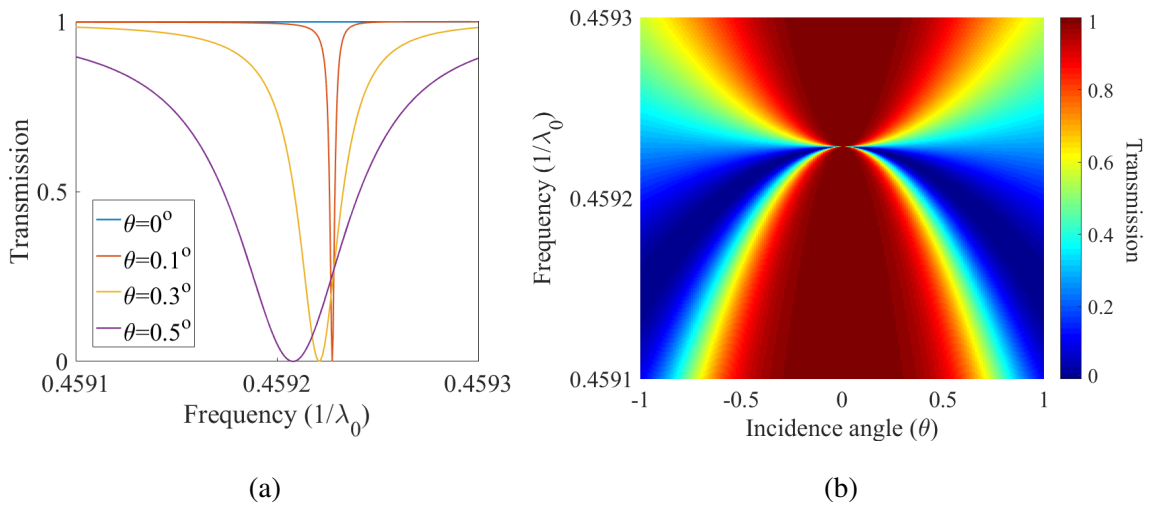


FIG. 3.6: Reproduction of the transmission efficiency plots for TM-polarized incidence on 2D gratings shown in Fig. 3.4b. Compare with (a) [9, Fig. 7c] and (b) [9, Fig. 7b]

Here, the entire matrix \mathbf{C} is considered to be unknown even though we do know that $\mathbf{I}^+ = \delta_0$ and $\mathbf{I}^- = \mathbf{0}$ in most cases. Next we obtain a matrix \mathbf{B} that can be used to find the incident fields such that

$$\mathbf{BC} = \mathcal{F}, \quad \text{or} \quad \mathbf{C} = \mathbf{B}^{-1}\mathcal{F}. \quad (3.15)$$

3.3.1 The big matrix for a single layer

To begin with a simple example, we first express \mathbf{B} for 1D gratings. The goal is to express the fields at every interface using the coefficients available in \mathbf{C} . For the first interface, from the incidence layer (at $z = 0^-$) we obtain

$$\begin{bmatrix} \mathbf{W}_1 & \mathbf{W}_1 \\ \mathbf{V}_1 & -\mathbf{V}_1 \end{bmatrix} \begin{bmatrix} \mathbf{I}^+ \\ \mathbf{R} \end{bmatrix} - \begin{bmatrix} \mathbf{W}_1 \\ -\mathbf{V}_1 \end{bmatrix} \mathbf{R} = \begin{bmatrix} \mathbf{E}_{\text{inc}} \\ \mathbf{H}_{\text{inc}} \end{bmatrix}. \quad (3.16a)$$

Looking at the same interface from the grating layer ($z = 0^+$) we obtain

$$- \begin{bmatrix} \mathbf{W}_1 & \mathbf{W}_1 \\ \mathbf{V}_1 & -\mathbf{V}_1 \end{bmatrix} \begin{bmatrix} \mathbf{I}^+ \\ \mathbf{R} \end{bmatrix} + \begin{bmatrix} \mathbf{W}_2 & \mathbf{W}_2\mathbf{X} \\ \mathbf{V}_2 & -\mathbf{V}_2\mathbf{X} \end{bmatrix} \begin{bmatrix} \mathbf{c}_2^+ \\ \mathbf{c}_2^- \end{bmatrix} = \begin{bmatrix} \mathbf{0} \\ \mathbf{0} \end{bmatrix}. \quad (3.16b)$$

Similarly, assuming no incidence from the transmission side, the fields at the second interface are,

$$- \begin{bmatrix} \mathbf{W}_2\mathbf{X} & \mathbf{W}_2 \\ \mathbf{V}_2\mathbf{X} & -\mathbf{V}_2 \end{bmatrix} \begin{bmatrix} \mathbf{c}_2^+ \\ \mathbf{c}_2^- \end{bmatrix} + \begin{bmatrix} \mathbf{W}_3 & \mathbf{W}_3 \\ \mathbf{V}_3 & -\mathbf{V}_3 \end{bmatrix} \begin{bmatrix} \mathbf{T} \\ \mathbf{0} \end{bmatrix} = \begin{bmatrix} \mathbf{0} \\ \mathbf{0} \end{bmatrix}, \quad (3.16c)$$

$$- \begin{bmatrix} \mathbf{W}_3 & \mathbf{W}_3 \\ \mathbf{V}_3 & -\mathbf{V}_3 \end{bmatrix} \begin{bmatrix} \mathbf{T} \\ \mathbf{0} \end{bmatrix} + \begin{bmatrix} \mathbf{W}_3 \\ \mathbf{V}_3 \end{bmatrix} \mathbf{T} = \begin{bmatrix} \mathbf{0} \\ \mathbf{0} \end{bmatrix}. \quad (3.16d)$$

The column matrices from (3.14) become $\mathbf{C} = [\delta_0 \quad \mathbf{R} \quad \mathbf{c}_2^+ \quad \mathbf{c}_2^- \quad \mathbf{T} \quad \mathbf{0} \quad \mathbf{R} \quad \mathbf{T}]^T$ and $\mathcal{F} = [\mathbf{E}_{\text{inc}} \quad \mathbf{H}_{\text{inc}} \quad \mathbf{0} \quad \mathbf{0} \quad \mathbf{0} \quad \mathbf{0} \quad \mathbf{0} \quad \mathbf{0}]^T$ in this case. Now if we arrange the layer eigenvector matrices from equations (3.16) such that

$$\mathbf{B} = \begin{bmatrix} \mathbf{W}_1 & \mathbf{W}_1 & \mathbf{0} & \mathbf{0} & \mathbf{0} & \mathbf{0} & -\mathbf{W}_1 & \mathbf{0} \\ \mathbf{V}_1 & -\mathbf{V}_1 & \mathbf{0} & \mathbf{0} & \mathbf{0} & \mathbf{0} & \mathbf{V}_1 & \mathbf{0} \\ -\mathbf{W}_1 & -\mathbf{W}_1 & \mathbf{W}_2 & \mathbf{W}_2 \mathbf{X}_2 & \mathbf{0} & \mathbf{0} & \mathbf{0} & \mathbf{0} \\ -\mathbf{V}_1 & \mathbf{V}_1 & \mathbf{V}_2 & -\mathbf{V}_2 \mathbf{X}_2 & \mathbf{0} & \mathbf{0} & \mathbf{0} & \mathbf{0} \\ \mathbf{0} & \mathbf{0} & -\mathbf{W}_2 \mathbf{X}_2 & -\mathbf{W}_2 & \mathbf{W}_3 & \mathbf{W}_3 & \mathbf{0} & \mathbf{0} \\ \mathbf{0} & \mathbf{0} & -\mathbf{V}_2 \mathbf{X}_2 & \mathbf{V}_2 & \mathbf{V}_3 & -\mathbf{V}_3 & \mathbf{0} & \mathbf{0} \\ \mathbf{0} & \mathbf{0} & \mathbf{0} & \mathbf{0} & -\mathbf{W}_3 & -\mathbf{W}_3 & \mathbf{0} & \mathbf{W}_3 \\ \mathbf{0} & \mathbf{0} & \mathbf{0} & \mathbf{0} & -\mathbf{V}_3 & \mathbf{V}_3 & \mathbf{0} & \mathbf{V}_3 \end{bmatrix}, \quad (3.17)$$

we find that Eq. (3.15) is satisfied. In fact \mathbf{B} is just an expression of the four parts of Eq. (3.16) in a single matrix equation.

3.3.2 The general case

From the definition of \mathbf{B} we find that each layer has its own smaller 4×2 sub-matrix embedded in \mathbf{B} . We denote these sub-matrices with a lowercase \mathbf{b}_ρ where ρ indicates the layer. We may now write,

$$\mathbf{b}_\rho = \begin{bmatrix} \mathbf{W}_\rho & \mathbf{W}_\rho \mathbf{X}_\rho \\ \mathbf{V}_\rho & -\mathbf{V}_\rho \mathbf{X}_\rho \\ -\mathbf{W}_\rho \mathbf{X}_\rho & -\mathbf{W}_\rho \\ -\mathbf{V}_\rho \mathbf{X}_\rho & \mathbf{V}_\rho \end{bmatrix}. \quad (3.18)$$

After arranging the sub-matrices \mathbf{b} inside \mathbf{B} , we add to \mathbf{B} the last two columns, which contain the eigenvector matrices for the reflected and transmitted waves.

To calculate the fields, we use the approach that was presented in section 2.2.5. There are many layers in the grating so that for Eq. (2.27), we have $\rho = 1, 2, \dots, L$. Hence, we must slightly modify $\Phi_\rho(z)$. The matrix \mathbf{C}_ρ contains the forward- and backward-travelling amplitude coefficients of the layer ρ at its starting and ending interface respectively. Hence, the z -coordinate for each layer must be corrected by subtracting the z -coordinate at the start of that layer. So our modified definition becomes,

$$\Phi_\rho(z) = \begin{bmatrix} \Phi_\rho(z - z_\rho) & \mathbf{0} \\ \mathbf{0} & \mathbf{X}_\rho \Phi_\rho(z_\rho - z) \end{bmatrix} \quad (3.19)$$

for $z_{\rho-1} < z < z_\rho$.

The rest of the process to calculate the fields is the same. For any point (x, z) , we first figure out the layer to which it belongs, after which all the fields can be computed by using Eq. (2.27) for that layer,

$$\Psi_\rho(x, z) = \Phi_x(x) \mathbf{M}_\rho \Phi_\rho(z) \mathbf{C}_\rho. \quad (3.20)$$

3.3.3 Results

To plot the fields for the structures shown in Fig. 3.4, we use the big matrix formulation. To find the Dirac point for the structures, we could use the S-matrix (Fig. 3.5) since the diffraction efficiencies calculated by the methods are consistent, and the S-matrix is faster. The results shown in Figs. 3.7 and 3.8 clearly show the expected accumulation of the fields at the Dirac point. Note the change in scale of the color plot.

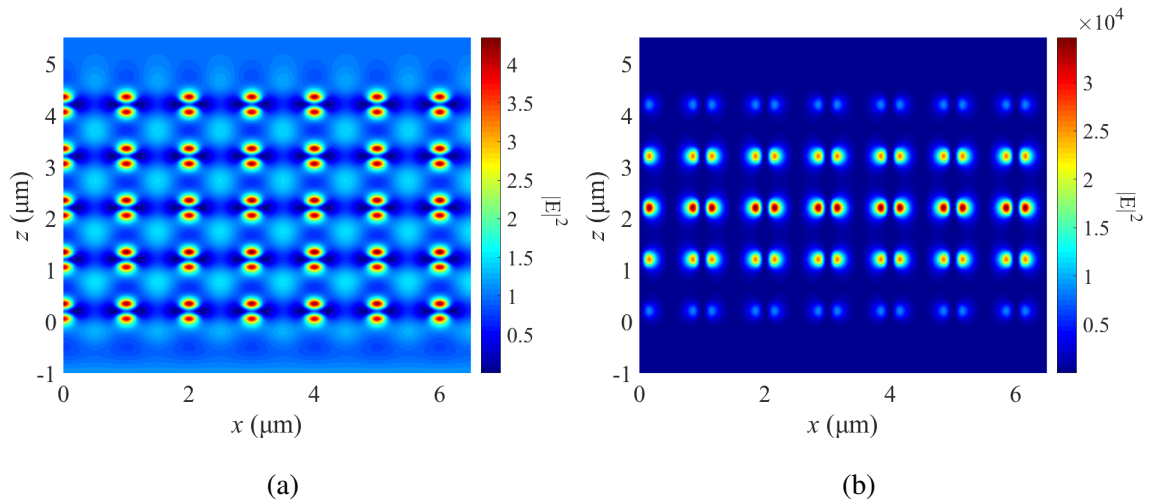


FIG. 3.7: Field distribution for the photonic structure in Fig. 3.4a with TE-polarized incidence. Electric field intensity at the Dirac point for **(a)** normal incidence and for **(b)** $\theta = 0.1^\circ$.

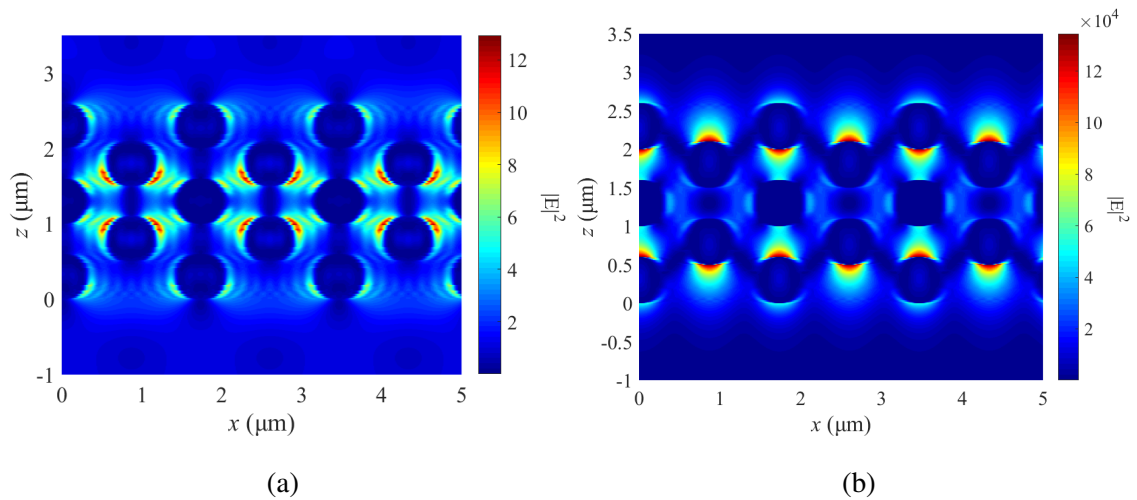


FIG. 3.8: Field distribution for the photonic structure in Fig. 3.4b with TM-polarized incidence. Electric field intensity at the Dirac point for **(a)** normal incidence and for **(b)** $\theta = 0.1^\circ$.

Chapter 4

3D GRATINGS

In this chapter, we further extend our algorithm. We will analyze a grating that is periodic in both the x - and y -directions, so that the permittivity can vary across three dimensions. Nearly any photonic structure can be analyzed using the methods developed in this section, but the period of the structure must still remain constant along the direction of propagation. Here, we will only discuss the solution for a single layer. Techniques developed in Chapter 3 can then be applied to study multiple layers. A rudimentary formulation was first developed by Nojonen and Turunen [4] in 1994. Later, the idea was improved by Li [5] and a correction for the Fourier series of the permittivity distribution was introduced that is similar to the correction that was described in Section 2.3.

We begin by taking a closer look at the geometry. Figure 4.1 shows an example of a three-dimensional (3D) grating. The grating profile has a thickness h , and the grating separates two semi-infinite dielectric media with refractive indices n_I for $z < 0$, and n_{II} for $z > h$.

The approach to calculate efficiencies and fields inside this structure remains similar to the methods used for a grating layer that we discussed in the Chapter 2. The Fourier series of the grating permittivity function is estimated and the resulting eigenvalue equation is solved once the boundary conditions are incorporated. Finally, the reflection and

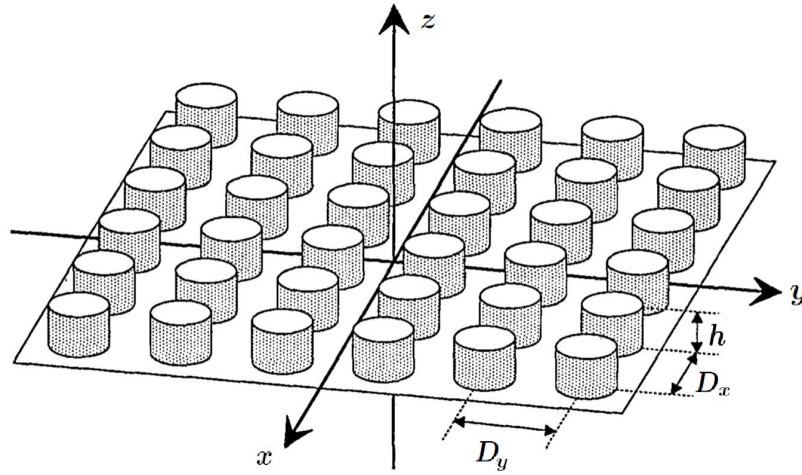


FIG. 4.1: Schematic representation of a doubly periodic, binary surface-relief grating [4, Fig. 1].

transmission coefficients are obtained. However, due to the bi-directional periodicity of the structure, the coefficients are two-dimensional.

4.1 Reflected and Transmitted Fields

If \mathbf{R}_{mn} and \mathbf{T}_{mn} are the reflected and transmitted field coefficients, the electric fields in the homogeneous regions \mathbf{E}_R and \mathbf{E}_T can be expressed as,

$$\mathbf{E}_R(\mathbf{r}) = \sum_{m,n} \mathbf{R}_{mn} \exp(j\mathbf{k}_{I,mn} \cdot \mathbf{r}), \quad (4.1a)$$

$$\mathbf{E}_T(\mathbf{r}) = \sum_{m,n} \mathbf{T}_{mn} \exp(j\mathbf{k}_{II,mn} \cdot \mathbf{r}), \quad (4.1b)$$

where N_x and N_y are odd, and m and n are integers in the range $[-(N_x - 1)/2, (N_x - 1)/2]$ and $[-(N_y - 1)/2, (N_y - 1)/2]$ respectively, where N_x and N_y are the number of diffraction orders that will be included in the calculations along the x - and y -direction respectively.

The wavevector $\mathbf{k}_{\rho,mn} = k_{xmn} \hat{\mathbf{x}} + k_{ymn} \hat{\mathbf{y}} - k_{\rho,zmn} \hat{\mathbf{z}}$ with

$$k_{xmn} = n_{\text{I}} k_0 \sin \theta \cos \phi + 2\pi m / D_x, \quad (4.2a)$$

$$k_{ymn} = n_{\text{I}} k_0 \sin \theta \sin \phi - 2\pi n / D_y, \quad (4.2b)$$

and

$$k_{\rho,zmn} = [(k_0 n_{\rho})^2 - k_{xmn}^2 - k_{ymn}^2]^{1/2}. \quad (4.2c)$$

The magnetic fields can be obtained, using Eq. (1.5a) which yields,

$$\mathbf{H}_R(\mathbf{r}) = \frac{j}{k_0} \sum_{m,n} \mathbf{k}_{\text{I},mn} \times \mathbf{R}_{mn} \exp(j\mathbf{k}_{\text{I},mn} \cdot \mathbf{r}), \quad (4.3a)$$

$$\mathbf{H}_T(\mathbf{r}) = \frac{j}{k_0} \sum_{m,n} \mathbf{k}_{\text{II},mn} \times \mathbf{T}_{mn} \exp(j\mathbf{k}_{\text{II},mn} \cdot \mathbf{r}). \quad (4.3b)$$

The matrices, with elements \mathbf{R}_{mn} , \mathbf{T}_{mn} , and $\mathbf{k}_{\rho,mn}$, of size $N_x \times N_y$ are reshaped to column vectors, which reduces the two coefficients to a single index $p = nN_x + m$. These matrices are now of size $N_t \times 1$ where the total number of orders is $N_t = N_x N_y$, and the index p is an integer in $[-(N_t - 1)/2, (N_t - 1)/2]$.

Due to the orthogonality of modes, we can find the z -component from the x - and y -components of the field amplitude coefficients using $\mathbf{k}_{\rho} \cdot \mathbf{C}_p = 0$. So we define the amplitude coefficient matrices as a column matrix $\mathbf{C} = [\mathbf{C}_x \quad \mathbf{C}_y]^T$. A similar treatment is given to the matrices for the fields \mathbf{E} and \mathbf{H} . Hence, we may express the magnetic field in region ρ as

$$\mathbf{H}_{\rho} = \mathbf{V}_{\rho} \mathbf{E}_{\rho}, \quad (4.4)$$

where

$$\mathbf{V} = \begin{bmatrix} \mathbf{V}_{xx} & \mathbf{V}_{xy} \\ \mathbf{V}_{yx} & \mathbf{V}_{yy} \end{bmatrix}. \quad (4.5)$$

The (p, p) elements of the constituent diagonal matrices become

$$V_{xx,p} = j \frac{k_{xp} k_{yp}}{k_0 k_{zp}}, \quad V_{xy,p} = j \frac{k_{yp}^2 + k_{zp}^2}{k_0 k_{zp}}, \quad (4.5a)$$

$$V_{yx,p} = j \frac{k_{xp}^2 + k_{zp}^2}{k_0 k_{zp}}, \quad V_{yy,p} = -V_{xx,p}. \quad (4.5b)$$

We also define the diagonal matrix \mathbf{K}_y with the elements $K_{yq} = j k_{yq} / k_0$ and \mathbf{K}_x is defined in Eq. (2.7).

4.2 Fourier transforms of the permittivity function

In order to take into consideration the correct rules for transforming a product of two functions that we presented in Section 2.3.2, we must define some additional matrices for the Fourier series of the permittivity. The permittivity is now a function of both x and y and has to be transformed in both directions, so that

$$\epsilon_{m,n} = \frac{1}{D_x D_y} \int_0^{D_y} \int_0^{D_x} \epsilon(x, y) \exp \left[-j2\pi \left(\frac{mx}{D_x} + \frac{ny}{D_y} \right) \right] dx dy, \quad (4.6)$$

where m, n go from $-(N_\ell - 1)$ to $(N_\ell - 1)$ along their respective dimensions $\ell = x, y$. The coefficients are then arranged in an $N_t \times N_t$ Toeplitz matrix $[[\epsilon]]_{p,q} = [[\epsilon]]_{mn,jl} = \epsilon_{m-j, n-l}$ where p and q are the 1D indices that are obtained by rearranging the 2D indices mn and jl as $p = nN_x + m$ and $q = lN_y + j$.

Analytical expressions for two-dimensional structures are not generally available, but

the FFT makes computation of Fourier coefficients relatively straightforward. To apply it to a structure, we first determine the number of equidistant sampling points in a single period along both the directions of periodicity. If the structure is sampled at NN_x and NN_y points along x - and y -directions respectively, the permittivity function $\epsilon(x, y)$ of a single period may be arranged in a $NN_x \times NN_y$ matrix. The FFT is applied to this matrix along both dimensions and only the central $-(N_l - 1)$ to $(N_l - 1)$ orders along either direction are considered in the later calculations. The elimination of higher order terms contributes to minimizing the error while the use of large number of sampling points makes it possible to obtain a greater spatial resolution when defining the permittivity distribution.

Two dimensions also complicates the imposition of the continuity condition for the product $\epsilon\mathbf{E}$. Since the field E_x is discontinuous along the x -direction, and the field E_y is discontinuous along the y -direction, we must transform the permittivity in x using the inverse rule for a product of type ϵE_x , while for ϵE_y we must transform the permittivity in y using the inverse rule. We now define notations which were introduced by Li [5]. The 1D transforms in x and y are denoted using $[\cdot]$ and $[\cdot]$ respectively.

$$[\epsilon]_{mn} = \frac{1}{D_x} \int_0^{D_x} \epsilon(x, y) \exp \left[-j2\pi \frac{(m-n)x}{D_x} \right] dx, \quad (4.7a)$$

$$[\epsilon]_{mn} = \frac{1}{D_y} \int_0^{D_y} \epsilon(x, y) \exp \left[-j2\pi \frac{(m-n)y}{D_y} \right] dy. \quad (4.7b)$$

Hence the quantities $[\zeta]^{-1}$ and $[\zeta]^{-1}$ are the algebraic inverses of the Fourier domain inverse permittivity matrices. Applying the transform in the remaining dimension to these matrices yields the required permittivity components that have been transformed using the inverse rule in only one direction. Explicitly, we find

$$[[\epsilon]]_{mn, jl} = \{ \{ [\zeta]^{-1} \}_{mj} \}_{nl} = \frac{1}{D_y} \int_0^{D_y} \{ [\zeta]^{-1} \}_{mj}(y) \exp \left[-j2\pi \frac{(n-l)y}{D_y} \right] dy, \quad (4.8a)$$

$$[\epsilon]_{mn,jl} = [\{\zeta\}^{-1}]_{mj}{}_{nl} = \frac{1}{D_x} \int_0^{D_x} \{\zeta\}^{-1}(x) \exp \left[-j2\pi \frac{(n-l)x}{D_x} \right] dx. \quad (4.8b)$$

4.3 The Eigenvalue Equation

Inside the grating structure, Eq. (1.5) defines the behaviour of the fields. Writing the individual components of these equations and eliminating the z -component, we obtain

$$\begin{aligned} \partial_z E_x &= k_0 H_y + \partial_x [(k_0 \epsilon)^{-1} (\partial_x H_y - \partial_y H_x)], \\ \partial_z E_y &= -k_0 H_x + \partial_y [(k_0 \epsilon)^{-1} (\partial_x H_y - \partial_y H_x)], \\ \partial_z H_x &= k_0 \epsilon E_y + \partial_x [(k_0)^{-1} (\partial_x E_y - \partial_y E_x)], \\ \partial_z H_y &= -k_0 \epsilon E_x + \partial_y [(k_0)^{-1} (\partial_x E_y - \partial_y E_x)]. \end{aligned} \quad (4.9)$$

Using the same matrix rearrangement and permittivity transforms that we introduced before, these equations can be reduced to concise matrix equations

$$\partial_z \mathbf{E} = k_0 \begin{bmatrix} -\mathbf{K}_x [\epsilon]^{-1} \mathbf{K}_y & \mathbf{I} + \mathbf{K}_x [\epsilon]^{-1} \mathbf{K}_x \\ -\mathbf{I} - \mathbf{K}_y [\epsilon]^{-1} \mathbf{K}_y & \mathbf{K}_y [\epsilon]^{-1} \mathbf{K}_x \end{bmatrix} \mathbf{H} = k_0 \mathbf{F} \mathbf{H}, \quad (4.10a)$$

$$\partial_z \mathbf{H} = k_0 \begin{bmatrix} -\mathbf{K}_x \mathbf{K}_y & [\epsilon] + \mathbf{K}_x^2 \\ -[\epsilon] - \mathbf{K}_y^2 & \mathbf{K}_y \mathbf{K}_x \end{bmatrix} \mathbf{E} = k_0 \mathbf{G} \mathbf{E}. \quad (4.10b)$$

Eliminating \mathbf{H} , we arrive at the eigenvalue equation

$$\partial_z^2 \mathbf{E} = k_0^2 \mathbf{F} \mathbf{G} \mathbf{E}. \quad (4.11)$$

Hence, setting $\mathbf{A} = \mathbf{F} \mathbf{G}$ we can use the same ideas that were developed in the previous sections. As before, we find that $\mathbf{\Gamma}$ is a diagonal matrix with the square root of the eigen-

values γ_m of \mathbf{A} . The columns of \mathbf{W} are the propagating electric field modes in the grating region and the magnetic field modes \mathbf{V} can be obtained from Eq. (4.10a) or Eq. (4.10b). However, it is preferable to use

$$\mathbf{V} = -\mathbf{GW}\mathbf{\Gamma}^{-1}, \quad (4.12)$$

since it only requires the inversion of a diagonal matrix.

The different layers of the structure can now be combined using either approach discussed in Chapter 3. Finally, we note that $\mathbf{R} = \begin{bmatrix} \mathbf{R}_x & \mathbf{R}_y & \mathbf{R}_z \end{bmatrix}^T$ and $\mathbf{T} = \begin{bmatrix} \mathbf{T}_x & \mathbf{T}_y & \mathbf{T}_z \end{bmatrix}^T$ also have a z -component that must be considered when calculating the efficiencies. Due to the orthogonality of modes, we find that

$$k_{Iz,p}R_{z,p} = k_{xp}R_{x,p} + k_{yp}R_{y,p}, \quad (4.13a)$$

$$-k_{IIz,p}T_{z,p} = k_{xp}T_{x,p} + k_{yp}T_{y,p}. \quad (4.13b)$$

4.4 Fields in 3D

As discussed previously, to obtain a picture of the fields inside the structure the big matrix approach must be used. The arrangement of eigenmatrices \mathbf{W} and \mathbf{V} to form \mathbf{B} is the same as shown in Section 3.3. However, to obtain the fields from the amplitude coefficients, we must slightly modify the procedure described in Section 2.2.5.

The $\mathbf{\Psi}$ matrix should now contain all 3 components of the magnetic and electric fields, so that $\mathbf{\Psi} = \begin{bmatrix} \mathbf{E}_x & \mathbf{E}_y & \mathbf{E}_z & \mathbf{H}_x & \mathbf{H}_y & \mathbf{H}_z \end{bmatrix}^T$. For the added z -components we must define \mathbf{W}_z and \mathbf{V}_z . From Maxwell's equations, we have

$$k_0\epsilon E_z = \partial_x H_y - \partial_y H_x, \quad (4.14a)$$

$$k_0 H_z = \partial_x E_y - \partial_y E_x, \quad (4.14b)$$

from which we obtain

$$\mathbf{W}_z = [\epsilon]^{-1} \begin{bmatrix} -\mathbf{K}_y & \mathbf{K}_x \end{bmatrix} \mathbf{V}, \quad (4.15a)$$

$$\mathbf{V}_z = \begin{bmatrix} -\mathbf{K}_y & \mathbf{K}_x \end{bmatrix} \mathbf{W}. \quad (4.15b)$$

Using these definitions, the \mathbf{M} matrix to calculate the field amplitude coefficients now becomes

$$\mathbf{M} = \begin{bmatrix} \mathbf{W} & \mathbf{W} \\ \mathbf{W}_z & -\mathbf{W}_z \\ \mathbf{V} & -\mathbf{V} \\ \mathbf{V}_z & \mathbf{V}_z \end{bmatrix}. \quad (4.16)$$

The phase matrices are similar to ones used in section 2.2.5. The only change is the introduction of $\Phi_y(y)$ which is required due to the periodicity in y . Thus, the fields at any point in or around a structure simulated using this algorithm can be calculated as

$$\Psi(x, y, z) = \Phi_x(x) \Phi_y(y) \mathbf{M} \Phi_z(z) \mathbf{C}. \quad (4.17)$$

Chapter 5

A NOVEL METAMATERIAL ABSORBER

5.1 Introduction

Research in electromagnetic absorbers has a long history, dating back to the Salisbury absorber in 1952 [15]. The development of negative refractive index metamaterials was a breakthrough in this technology. Negative index materials were first conceived by Vesalago in 1968 [16], but it was not until 2000 that an experimental demonstration was obtained [17]. Subwavelength structures to produce a desired electromagnetic response in materials and devices continues to be a subject of considerable interest. Along with many possible exotic electromagnetic effects, metamaterials can be optimized for perfect absorption. The first such metamaterial absorber was developed in 2008 [18], experimentally achieving 88% absorption at microwave frequencies. Similar absorbers in the terahertz (THz) [19], infrared (IR) [20] and visible [21] regions followed soon thereafter. The applications of these materials are widespread and include solar light harvesting [22], thermophotovoltaic cells [23], selective thermal emitters [24], optoelectronic devices [25], plasmonic sensors [26], and stealth applications [27]. The first generation of metamaterial absorbers was based on split ring resonance or electric ring resonance mechanisms, but this approach is difficult to implement in practice as the wavelength becomes shorter. More recently, based on a better understanding of photonic crystals and nano-scale fabrication, new and

improved metamaterials to obtain specialized absorption spectra across a wider frequency range have been obtained. Polarization-independent, ultra-broadband absorption, which is the focus of this study, has been achieved in the gigahertz (GHz) [28] and terahertz (THz) [29] regime using metamaterials. However, producing similar effects in the visible and near-IR regions using efficient and cost-effective means is still a challenge. This paper describes a realistic approach to meet this challenge.

Recent studies into stratified metal-dielectric metamaterials have uncovered an efficient means of absorbing light at ultraviolet to near-infrared wavelengths [30, 31]. Consider a periodic sequence of elementary cells comprised of a thin metal layer sandwiched between two identical dielectric layers. Such a stratified, symmetric elementary cell acts as an equivalent bulk material with a single effective characteristic impedance and Bloch wave vector [32]. If the impedance of these metamaterials is matched to that of free space (incidence medium), all incident radiation will enter the material. The metal layers then absorb the radiation through ohmic loss [30]. Any number of the elementary cells may be stacked on top of each other, depending on the thickness and absorption requirements, as shown in Fig. 5.1a. The fabrication of these metamaterials can be achieved using simple, low-cost techniques like thermal evaporation or standard sputtering [33].

Impedance-matched metamaterials are inherently non-resonant absorbers, active over a broad bandwidth; however, the reflectivity of the metal layers dominates over the absorption as we venture deeper into the infrared region. In such a case, it seems reasonable to hypothesize that an effective anti-reflection coating would further improve the bandwidth and peak absorption. One of the ways to reduce reflection without adding more layers or compromising on the impedance matching is by imprinting “moth-eye” structures, shown schematically in Fig. 5.1b, through the top few elementary cells.

In the 1960s [34], it was discovered that corneal nipple patterns in the eyes of insects, and more specifically nocturnal moths, help them see clearly in the dark while also

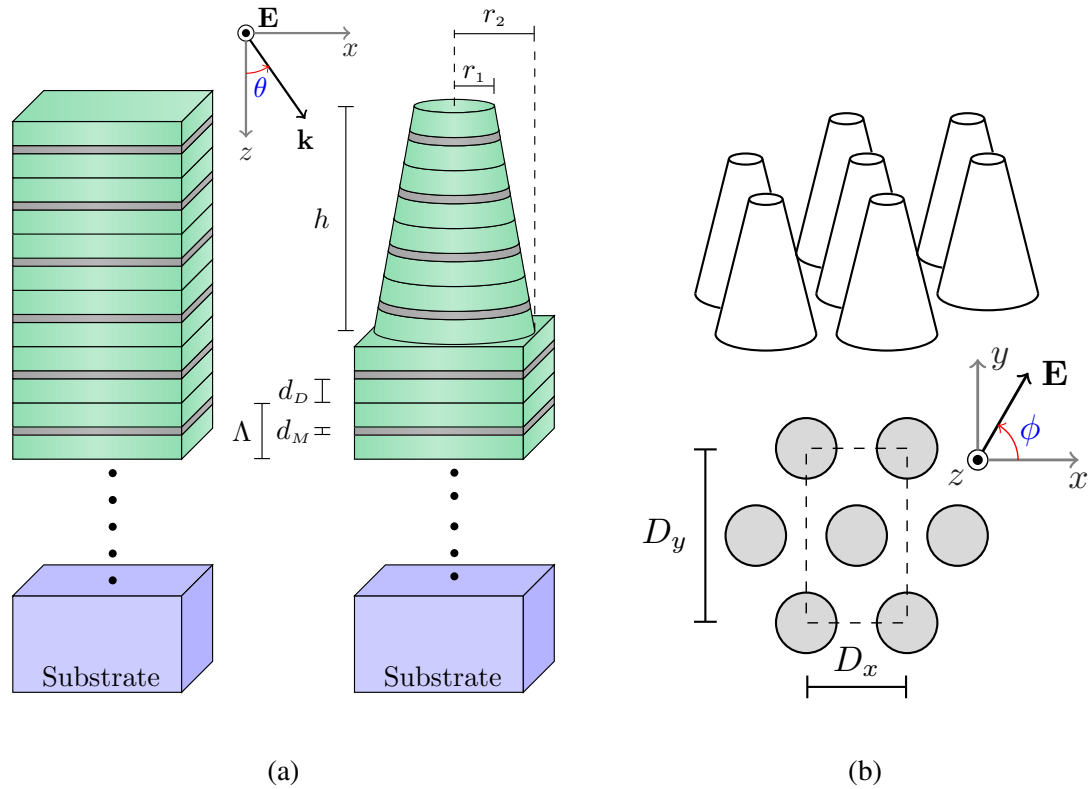


FIG. 5.1: Schematic illustrations of the metamaterials and incidence geometry. **(a)** Lateral view of impedance matched metal-dielectric metamaterials with a flat surface (left) and moth-eye surface (right). The elementary cell has a period Λ , and it consists of a metal layer of thickness d_M sandwiched between dielectric layers of thickness d_D . For the truncated conical pillars that form the moth-eye surface (right), the variables r_1 and r_2 are the radius at the top and bottom respectively and h is the height of the pillars. The geometry for TE-polarized incidence is also shown. **(b)** Top and 3D view of moth-eye surfaces obtained by arranging the truncated conical pillars in a triangular lattice with periods D_x and $D_y = \sqrt{3}D_x$ in the x - and y -directions respectively. The polarization angle ϕ is shown here for normal incidence.

avoiding predation [35]. Later, with the advent of better fabrication technology, biomimetic structures based on this design were found to be effective in reducing Fresnel reflections at optical interfaces [36]. These moth-eye surfaces have recently been demonstrated to reduce coupling losses at the end faces of optical fibers [37] as well as the reflection glare from modern electronic displays [38]. They can be imprinted on an existing material using laser writing [39] or nanoimprint lithography [40] and directly imprinted on flat impedance-matched metamaterials.

In this study, we approximate these structures as truncated cones, shown in Fig. 5.1a, that are arranged as shown in Fig. 5.1b. At wavelengths that are longer than the dimensions of the moth-eye structures, these surfaces can be simply modeled and reduce reflection by producing a gradual refractive index gradient at the interface. However, when the dimensions of these structures are on the order of the wavelength of the incident light, full-wave computational methods must be employed in order to model their reflection, transmission and absorption properties accurately. For the results that follow, we have used our own implementation of the rigorous coupled-wave algorithm (RCWA) that was discussed in the preceding chapters. The MATLAB implementation has been included in Appendix A.

In the following section, we discuss the design of an improved metamaterial by combining the concept of impedance-matched metallo-dielectric metamaterials [30] and AR moth-eye structures. We demonstrate the possibility of achieving broad-angle, polarization independent absorbers over a broad wavelength range that spans 500 nm to 6 μm .

5.2 Results and Discussion

We next show that imprinting moth-eye structures on the first few layers of impedance matched metamaterials significantly broadens the material's absorption spectrum. We model two impedance-matched metal-dielectric metamaterials, one with a moth-eye sur-

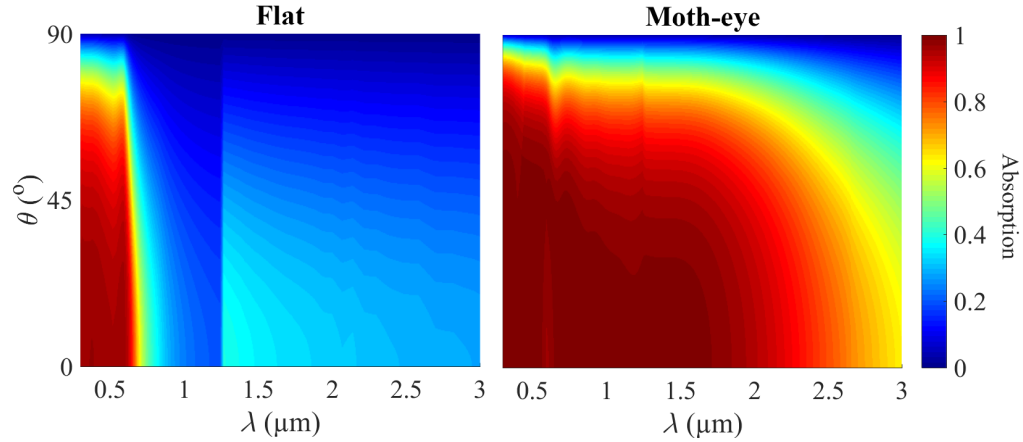


FIG. 5.2: The absorption spectrum for the Cu-based metamaterial that we consider with TE-polarized incidence ($\phi = 90^\circ$). The elementary cell in this metamaterial has metal layers of thickness, $d_M = 10$ nm and SiO_2 layers of thickness, $d_D = 30$ nm. The moth-eye surface has a height $h = 280$ nm, periods $D_x = 300$ nm and $D_y = 520$ nm, and radii $r_1 = 50$ nm and $r_2 = 145$ nm.

face and the other with a flat surface. We simulate the effects of monochromatic incidence from $\theta = 0^\circ$ to $\theta \approx 90^\circ$ on these metamaterials and plot the absorption spectrum as shown in Figs. 5.2 and 5.3.

The metamaterial with a flat surface is the same as sample 2 from [30]. It consists of 10 repetitions of the elementary cell made up of a 10 nm layer of copper (Cu) between 30 nm layers of SiO_2 ($\Lambda = 70$ nm) on a quartz substrate with an index of refraction $n = 1.52$. The moth-eye metamaterial has its first 4 repetitions of the elementary cell imprinted into truncated pillars and arranged on a triangular lattice to form the moth-eye surface. The lattice periods are chosen as $D_x = 300$ nm and $D_y = 520$ nm, while the radii at top and bottom are taken as 50 nm and 145 nm respectively. The periodicity, height, and radii of the pillars can all be modified in principle to tune the absorption spectrum.

Along with Cu, we also consider metamaterials with tungsten (W) as the metal

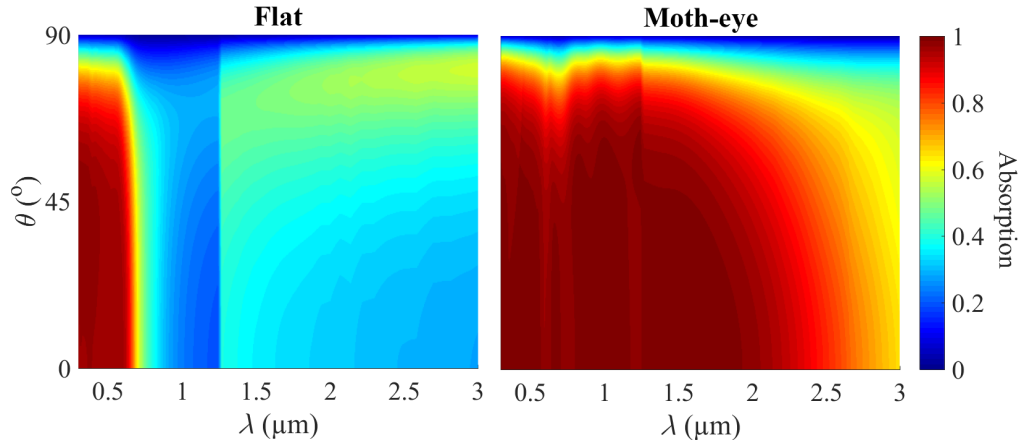


FIG. 5.3: Same as Fig. 5.2 with TM-polarization ($\phi = 0^\circ$).

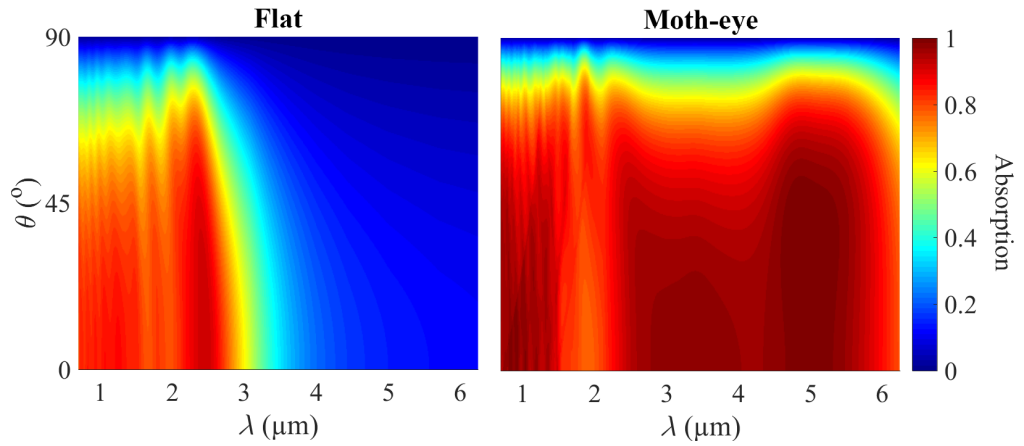


FIG. 5.4: The absorption spectrum for the W-based metamaterials that we consider with TE-polarized incidence. Structure parameters, $d_M = 5$ nm, $d_D = 75$ nm, $h = 620$ nm, $D_x = 834$ nm, $D_y = 1444$ nm, $r_1 = 236$ nm, and $r_2 = 383$ nm.

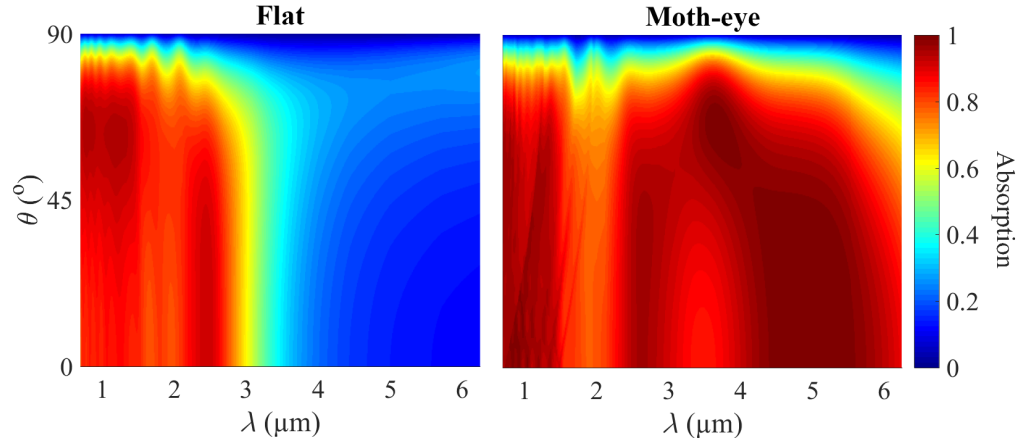


FIG. 5.5: Same as Fig. 5.4 with TM-polarization.

(Figs. 5.4 and 5.5). The elementary cell based on W is composed of a 5-nm layer of the metal surrounded by 75 nm layers of Ta_2O_5 . Since the flat metamaterial based on W is known to have a longer central wavelength and broader spectrum than the Cu-based metamaterial, the lattice periods are chosen to be $D_x = 834$ nm and $D_y = 1444$ nm. The radii are similarly adjusted with $r_1 = 236$ nm and $r_2 = 383$ nm. No substrate is present, and the output medium is air with an index of refraction $n = 1$.

We use the data of Palik [14] and Ordal *et al.* [41] to obtain the dispersion of Cu and W respectively. Since the thickness of the metal layers is on the order of the electron mean free path, the Fuchs-Sondheimer theory [42] should be used for the Drude model calculations. Hence, the data for the bulk metals has been adjusted for thin metal films using the methodology elaborated in [30]. The refractive index for SiO_2 comes from the Sellmeier equation [43] and for Ta_2O_5 from [44]. The plots for the metamaterials with a flat surface closely match the results shown in Figs. 9 and 10 of [30], and the absorption spectrum with the moth-eye surfaces is greatly broadened as anticipated.

In Fig. 5.6, in order to better understand the impact of impedance matching and anti-reflection, we show the absorption for flat films and moth-eye structures that are entirely

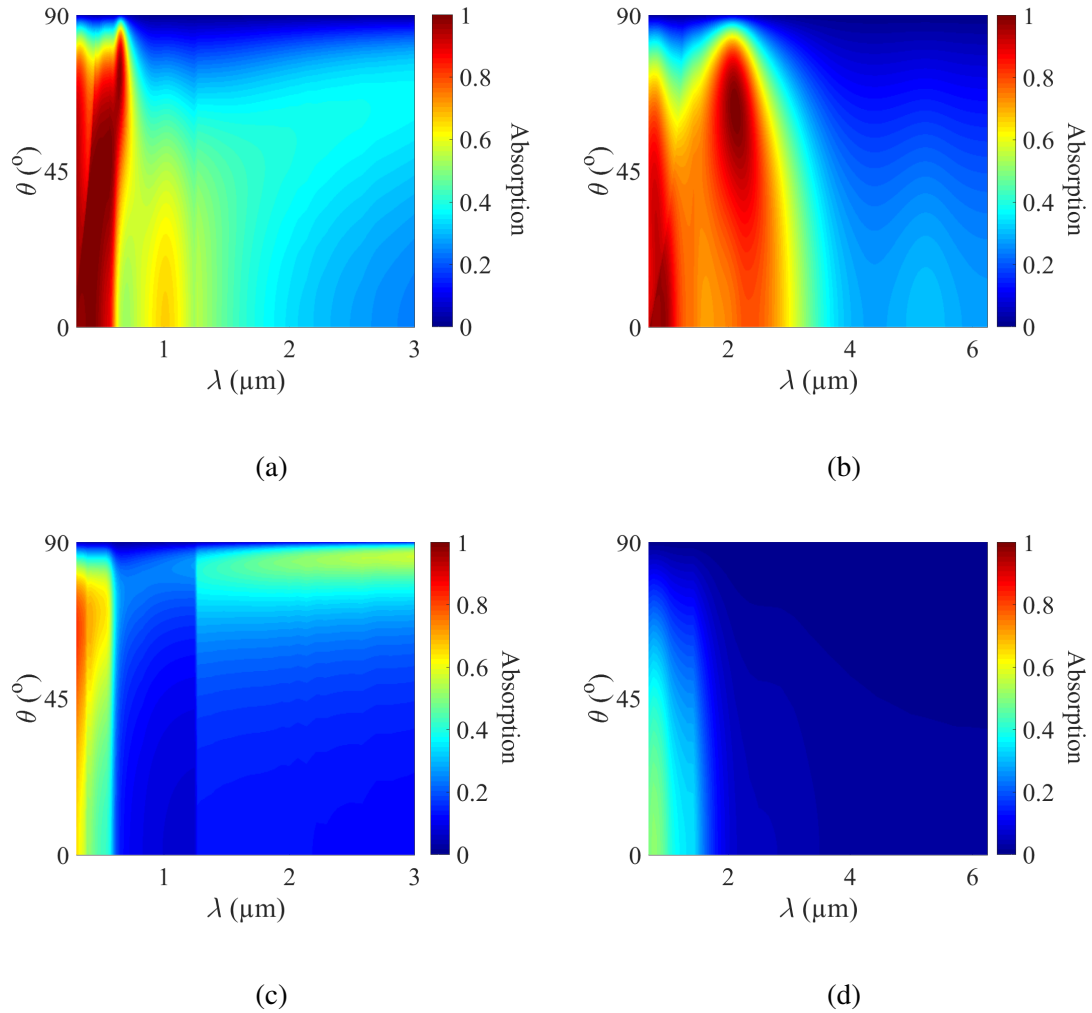


FIG. 5.6: The absorption spectrum for the non-impedance-matched all-metal films and moth-eye structures. **(a)** Moth-eye surfaces made entirely of Cu with TM-polarized incidence. **(b)** Moth-eye surfaces made entirely from W with TE-polarized incidence. **(c)** 700 nm thick Cu-film with TM-polarized incidence. **(d)** 1550 nm thick W-film with TE-polarized incidence. The dimensions for the moth-eye surfaces are outlined in Fig. 5.2 for (a) and Fig. 5.4 for (b) with a transmission region of the same metal. Transmission region for (c) and (d) is air.

composed of metal. The dimensions of these materials, like the thickness of the film, radii and periods of the moth-eyes are equivalent to their corresponding metal-dielectric structures. The results show a much weaker absorption profile for the metal films and no significant broadening with the metal moth-eye surfaces. We conclude that the ultra-broadband absorption that is shown in Figs. 5.2 to 5.5 is not just due to the metal or moth-eye surface, but is due to a combination of impedance-matched metal-dielectric metamaterials and the moth-eye surface. A clearer picture on how that happens can be obtained by examining the field distribution inside the metamaterials.

In Figs. 5.7 and 5.8, we show the intensity of the electric field and the ohmic loss [equal to $\text{Im}(\epsilon) |E|^2$] distribution within the metamaterials. We focus on two incident wavelengths each for the Cu-based and W-based metamaterials. These wavelengths are chosen such that the shorter of the two lies within the absorption spectrum of the flat as well as the moth-eye metamaterial. The other wavelength is absorbed only by the moth-eye metamaterial. We chose wavelengths of 0.5 μm , and 1.2 μm for the Cu-based metamaterials, and we choose 2.5 μm , and 5 μm for the W-based metamaterials.

In the flat metamaterial, the maximum attenuation always occurs in the first metal layer and successively decreases with each layer. Moreover, the peak absorption in the first metal layer is not significantly reduced even at the longer wavelength. However, the penetration is reduced because the first layer now reflects much of the light, and the energy carried by the light never reaches the other metal layers (shown by the broken lines in Figs. 5.7 and 5.8). Hence, the total absorption is reduced.

For the moth-eye surface, we look at the fields in a plane dividing the pillars in two vertical halves. The solid line traces the projection of the truncated pillars on this plane. In this case, the moth-eye surface act like a lens, focusing the incident energy at just a few spots inside the structure. Hence, a greater amount of energy passes through the metal, which produces higher loss that is also heavily concentrated in a few layers.

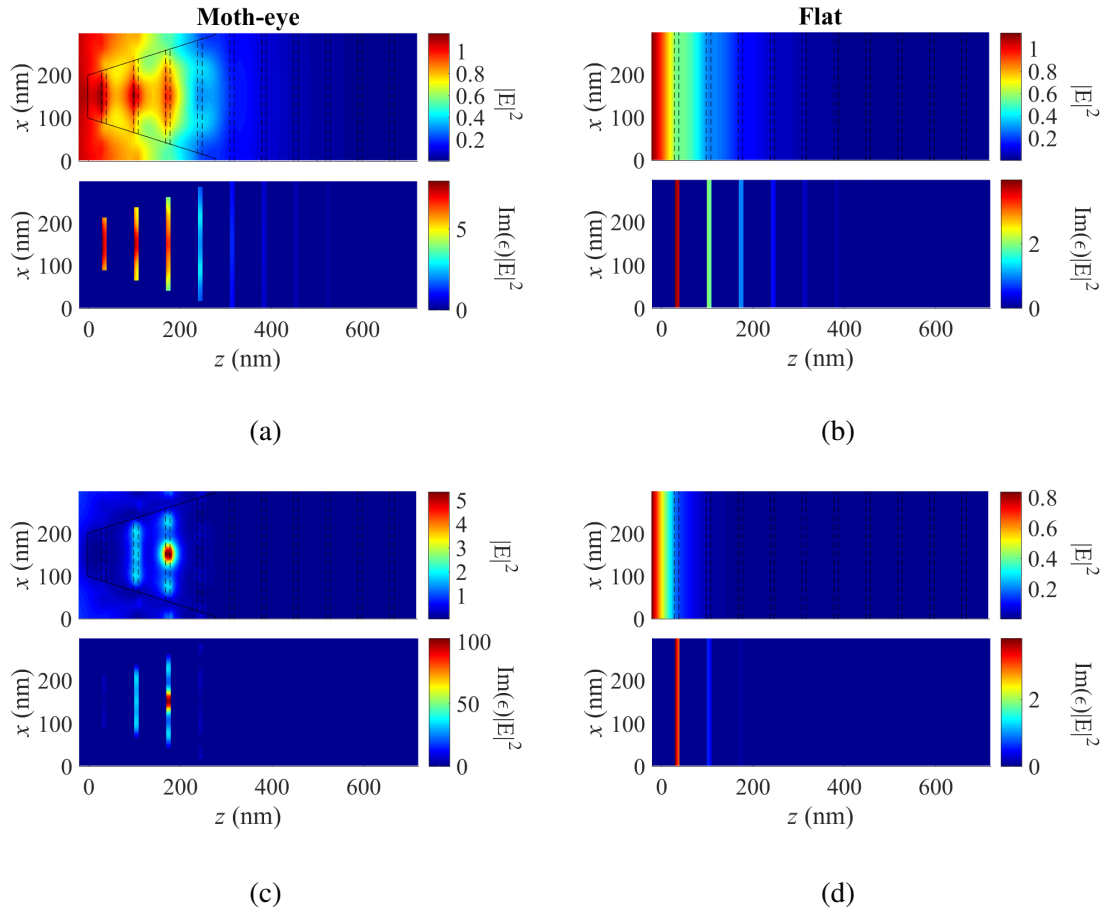


FIG. 5.7: Electric field intensity and ohmic loss distribution for Cu-based metamaterials. **(a)** $\lambda = 0.5 \mu\text{m}$, absorption $> 99\%$. **(b)** $\lambda = 0.5 \mu\text{m}$, absorption $\approx 95\%$. **(c)** $\lambda = 1.2 \mu\text{m}$, absorption $\approx 99\%$. **(d)** $\lambda = 1.2 \mu\text{m}$, absorption $\approx 20\%$.

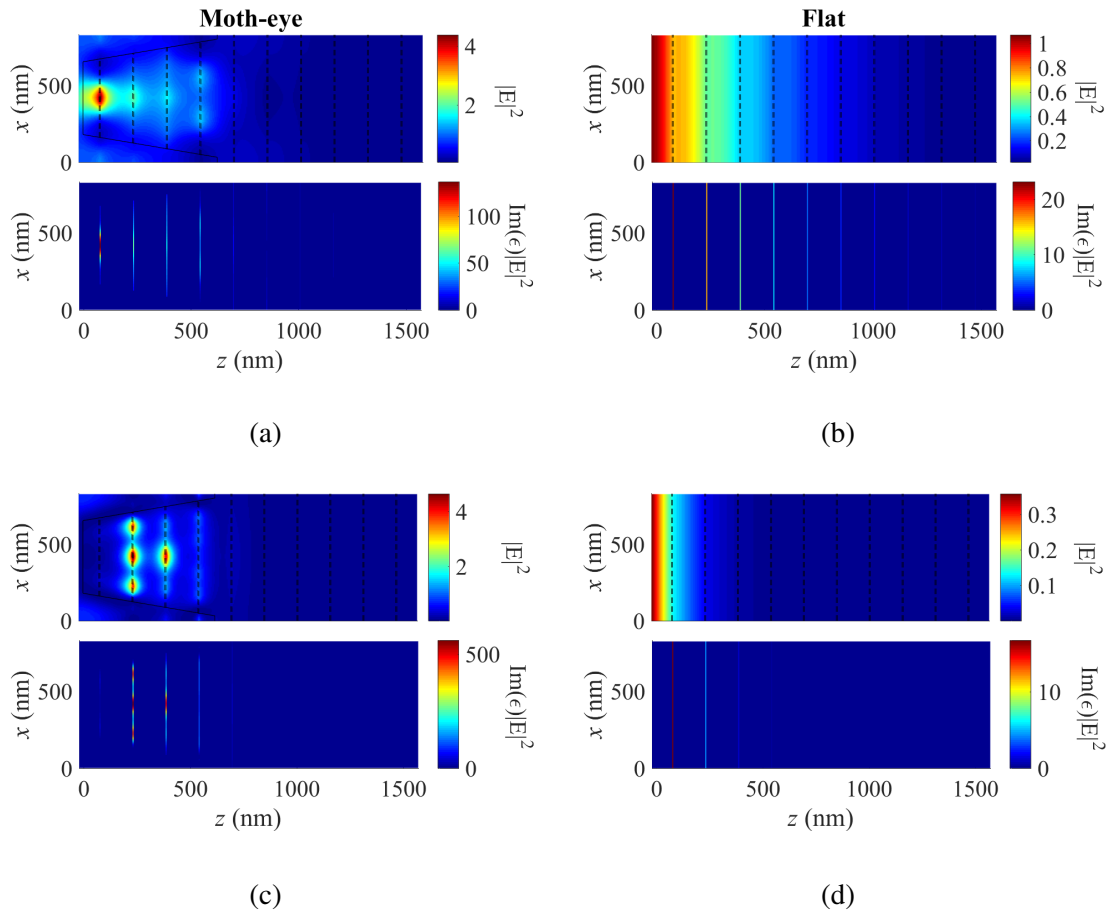


FIG. 5.8: Electric field intensity and ohmic loss distribution for W-based metamaterials. **(a)** $\lambda = 2.5 \mu\text{m}$, absorption $\approx 90\%$. **(b)** $\lambda = 2.5 \mu\text{m}$, absorption $\approx 90\%$. **(c)** $\lambda = 5 \mu\text{m}$, absorption $> 99\%$. **(d)** $\lambda = 5 \mu\text{m}$, absorption $\approx 15\%$.

5.3 Conclusion

We have proposed and computationally analyzed a novel approach to achieve absorption over a wide spectrum by combining two independent mechanisms: (a) metal-dielectric impedance-matched metamaterials and (b) anti-reflective moth-eye structures. The analysis was done using the RCWA [1, 5] method, which was developed in-house and validated by comparison with experimental results. Our implementation was then applied to the proposed designs.

By testing the hypothesis on structures that we designed using the metals Cu and W, we found that moth-eye surfaces imprinted on impedance-matched metal-dielectric metamaterials can greatly broaden the absorption bandwidth of the corresponding flat metamaterial. By simulating the absorption spectrum of all metal films and moth-eye structures, we also confirmed that neither the metal nor the moth-eye structures alone are the cause of the broadening. Finally, by generating a visual representation of the electric field distribution inside the metamaterials, we provided an understanding of the loss mechanism behind this phenomenon.

We have computationally demonstrated a practical and cost-efficient approach to obtain polarization-independent, non-resonant, broadband absorption. Similar to flat impedance-matched metamaterials, the absorption of the moth-eye metamaterial is also independent of the substrate and can be used as a thin film to cover other materials. The fabrication of planar multilayer materials can be achieved through standard sputtering or thermal evaporation techniques [33], and fabrication of moth-eye structures based on nanopillars with dimensions on the order of a few hundred nm is well within the reach of current nanolithography techniques. Moreover, while we have studied metals here, the same concepts and designs can be exploited using semiconductor materials in their absorption band. In this case, instead of being dissipated through ohmic losses in the metal, the light can be

harvested to create electron-hole pairs in the semiconductor material for efficient infrared detectors, night vision cameras, or solar cell applications.

Appendix A

MATLAB SCRIPTS

We present two example scripts that we used to simulate the response of the moth-eye metamaterial absorber discussed in Chapter 5. Listing A.1 plots the absorption spectrum of the W-based moth-eye metamaterials shown in Fig. 5.4 and the script in A.2 recreates the field distribution for Cu-based moth-eye metamaterial at wavelength of 500 nm Fig. 5.7a.

Listing A.1: MATLAB script to recreate Fig. 5.4

```
%% Inputs and Structure Parameters

y = 700.1:10:6250.1; % Range of wavelength in nm

% Angles
th = 0:0.25:89.75; % Incidence Angle (deg)
phi = 0; % Angle between 'x' axis and plane of incidence (deg)
psi = 90; % Polarization angle (deg) 0 -> TM, 90 -> TE

% Unit cell parameters
mlt = 2.78; % Scaling factor for the hexagonal unit cell
D_x = 300; % Length of one period in 'x'
D_x = 2*round(D_x*mlt/2); % Scaled and rounded to nearest even number
D_y = 2*round(sqrt(3)*D_x/2); % Length of one period in 'y'
```

```

% Metal-dielectric metamaterials
D_m = 5; % Thickness of metal layer in 'z'
D_d = 75; % Thickness of dielectric layer in 'z'
NN_z = 6; % Number of uncarved unit cells (after the moth-eyes)
% NN_z = 10; for uncarved % NN_z = 0; for metal moth-eyes on metal
    substrate

% Moth-eye Structures
N_m = 4; % = 0; for uncarved % Number of elementary cells carved into
    pillars
r_1 = 85*mlt; % Radius of pillars at top
r_2 = 138*mlt; % Radius of pillars at bottom
N_zd = 3; % Number of slices of the dielectric layer (calculates radius,
    increase for accuracy)
D_z = N_m*(2*D_d+D_m); % Thickness of moth-eye structure in 'z'
N_z = N_m*(2*N_zd+1); % Number of layers in one carved elementary cell
h_zd = D_d/N_zd; % Resolution in 'z' for carved dielectric layers
h_z = repmat([repmat(h_zd,1,N_zd),D_m,repmat(h_zd,1,N_zd)],1,N_m); %
    Height of each carved layer
z_1 = [0,cumsum(h_z(1:N_z-1))]; % 'z' coordinate of each carved layer
r_z = interp1([0,D_z-h_zd],[r_1,r_2],z_1); % Radius of pillars for each
    carved layer
N_l = N_z+3*NN_z+2; % Total layers

% Fourier modes to consider in calculations (ODD)
N_x = 9; %=1; for uncarved % Number of Fourier modes in x direction
N_y = 9; %=1; for uncarved % Number of Fourier modes in y direction
Nt = N_x*N_y;

% Preallocations
ky = 2*pi./y; % Wavenumbers

```

```

I = eye(Nt); II = eye(2*Nt); % Identity matrices
ZZ = zeros(2*Nt);
EPS = zeros(Nt,Nt,N_z);
EPSyx = zeros(Nt,Nt,N_z);
EPSxy = zeros(Nt,Nt,N_z);
W = zeros(2*Nt,2*Nt,N_1);
V = zeros(2*Nt,2*Nt,N_1);
X = zeros(2*Nt,2*Nt,N_1);
DEr = zeros(length(y),length(th),length(psi));
DEt = zeros(length(y),length(th),length(psi));

% Foruier mode numbers and arrays
mx = (-(N_x-1)/2:(N_x-1)/2)';
my = (-(N_y-1)/2:(N_y-1)/2);
m0x = (N_x+1)/2;
m0y = (N_y+1)/2;
m0 = (Nt+1)/2;

%% Wavelength based permittivity

% Metal (with thin layer correction)
load Tu.txt; % Taken from refractiveindex.info
Me = interp1(Tu(:,1),Tu,y/1000); % Interpolation of experimental data
Metal = (Me(:,2) + 1i*Me(:,3)).^2; Metal = Metal.';
kkk = D_m/19; % Thickness of W layer divided mean free path of W
kky = 1000*ky;
fi = (1./kkk+3/4*(1-1/12*kkk.^2).*expint(kkk)-3./(8*kkk.^2).*(1-exp(-kkk)
    ))-(5./(8*kkk)+1/16-kkk/16).*exp(-kkk).^-1;

wp = 0.79; % Plasma frequency in micron^-1
gamma = 39.79*10^-4; gammakk = gamma*fi/kkk;

```

```

epsDrude = 1-(wp^2)./((kky/(2*pi)).^2+1i*(kky/(2*pi))*gamma); % Drude
    model for the Bulk

epsDrudekk = 1-(wp^2)./((kky/(2*pi)).^2+1i*(kky/(2*pi))*gammakk); %
    Drude Model corrected for the thin layer

epsMetal = Metal-epsDrude+epsDrudekk;

% Dielectric
load Ta205_n.txt; load Ta205_k.txt; % Taken from refractiveindex.info
De = interp1(Ta205_n(:,1), [Ta205_n(:,2), Ta205_k(:,2)], y/1000);
eps_d = (De(:,1) + 1i*De(:,2)).^2;

%% Index profile of moth eye structures
% Build the moth-eye structure as a binary 3D matrix

indexProfLog = false(D_x,D_y,N_z);

% Hexagon vertice positions
centre = [D_x,D_y]/2;

for nn=1:N_z
    r = round(r_z(nn));
    % Pillars
    [rr,cc] = meshgrid(1:2*r+1);
    circ = (rr-1-r).^2+(cc-1-r).^2<=r^2;
    % Positioning the pillars
    indexProfLog((centre(1)-r):(centre(1)+r), (centre(2)-r):(centre(2)+r)
        ,nn) = circ;
    indexProfLog(1:r,1:r,nn) = indexProfLog(1:r,1:r,nn) | circ(r+2:2*r
        +1,r+2:2*r+1);

```



```

indexProfLog(1:r,D_y-r:D_y,nn) = indexProfLog(1:r,D_y-r:D_y,nn) |
    circ(r+2:2*r+1,1:r+1);
indexProfLog(D_x-r:D_x,D_y-r:D_y,nn) = indexProfLog(D_x-r:D_x,D_y-r:
    D_y,nn) | circ(1:r+1,1:r+1);
indexProfLog(D_x-r:D_x,1:r,nn) = indexProfLog(D_x-r:D_x,1:r,nn) |
    circ(1:r+1,r+2:2*r+1);
end

%% Begin loop in wavelength

for yy=1:length(y)
    uy = y(yy)/1000; % Wavelength in micron

    %% Structure Analysis

    % Permittivity and refractive indices
    n_1 = 1; % Refractive index of incidence medium
    n_3 = 1; % Refractive index of transmission medium
    % n_3 = conj(epsMetal(yy))^2; for metal as substrate/
    transmission medium
    e_m = epsMetal(yy); % Permittivity of metal for current
    wavelength
    e_d = eps_d(yy); % Permittivity of dielectric layer (Ta2O5)
    % e_d = e_m; for all metal moth-eyes
    e_f = 1; % Permittivity of material between pillars
    e_p = repmat([repmat(conj(e_d),N_zd,1);conj(e_m);repmat(conj(e_d)
        ),N_zd,1)],N_m,1);

    % Permittivity matrices for each layer
    indexProf = ones(D_x,D_y);
    for nn=1:N_z

```

```

indexProf(indexProfLog(:, :, nn)) = e_p(nn);
indexProf(~indexProfLog(:, :, nn)) = e_f;

eps_fft = fftshift(fft2(indexProf))/(D_x*D_y);
eps_mn = eps_fft(D_x/2+2-N_x:D_x/2+N_x, D_y/2+2-N_y:D_y
    /2+N_y);

for pp = 1:N_x
    for qq = 1:N_y
        EE = rot90(eps_mn(pp:pp+N_x-1, qq:qq+N_y
            -1), 2);
        EPS(pp+N_x*(qq-1), :, nn) = reshape(EE
            , 1, []);
    end
end

i_iepsx_mj = zeros(N_x, D_y, N_x);
iepsx_fft = fftshift(fft(indexProf.^(-1), [], 1), 1)/D_x;

for qq=1:D_y
    iepsx_m = iepsx_fft(D_x/2+2-N_x:D_x/2+N_x, qq);
    iepsx_mj = toeplitz(iepsx_m(N_x:2*N_x-1), flip(
        iepsx_m(1:N_x)));

    i_iepsx_mj(:, qq, :) = inv(iepsx_mj);
end

epsxy_fft = fftshift(fft(i_iepsx_mj, [], 2), 2)/D_y;
epsxy_mnj = epsxy_fft(:, D_y/2+2-N_y:D_y/2+N_y, :);

E4 = zeros(N_x, N_y, N_x, N_y);

```

```

for pp = 1:N_x
    for qq = 1:N_x
        E4(pp, :, qq, :) = toeplitz(epsxy_mnj(pp,
            N_y:2*N_y-1, qq), flip(epsxy_mnj(pp, 1:
            N_y, qq)));
    end
end

EPSxy(:, :, nn) = reshape(E4, [N_x*N_y, N_x*N_y]);

i_iepsy_n1 = zeros(D_x, N_y, N_y);
iepsy_fft = fftshift(fft(indexProf.^(-1), [], 2), 2)/D_y;

for pp=1:D_x
    iepsy_n = iepsy_fft(pp, D_y/2+2-N_y:D_y/2+N_y);
    iepsy_n1 = toeplitz(iepsy_n(N_y:2*N_y-1), flip(
        iepsy_n(1:N_y)));

    i_iepsy_n1(pp, :, :) = inv(iepsy_n1);
end

epsyx_fft = fftshift(fft(i_iepsy_n1, [], 1), 1)/D_x;
epsyx_mn1 = epsyx_fft(D_x/2+2-N_x:D_x/2+N_x, :, :);

E4 = zeros(N_x, N_y, N_x, N_y);

for rr = 1:N_y
    for ss = 1:N_y
        E4(:, rr, :, ss) = toeplitz(epsyx_mn1(N_x
            :2*N_x-1, rr, ss), flip(epsyx_mn1(1:N_x

```



```

k_m_zmn = conj((e_m*(k_0)^2*ones(Nt,1) - k_x_mn
    .^2 - k_y_mn.^2).^^(1/2));
k_3_zmn = conj(((n_3*k_0)^2*ones(Nt,1) - k_x_mn
    .^2 - k_y_mn.^2).^^(1/2));

K_x = li*diag(k_x_mn/k_0);
K_y = li*diag(k_y_mn/k_0);

%% Eigenmatrices

% Eigenvalue formulation for the grating region
for nn=1:N_z
    F11 = -K_x*(EPS(:, :, nn)\K_y);
    F12 = I + K_x*(EPS(:, :, nn)\K_x);
    F21 = -I - K_y*(EPS(:, :, nn)\K_y);
    F22 = K_y*(EPS(:, :, nn)\K_x);
    F = [F11 F12;F21 F22];

    G11 = -K_x*K_y;
    G12 = EPSyx(:, :, nn) + K_x^2;
    G21 = -EPSxy(:, :, nn) - K_y^2;
    G22 = K_x*K_y;
    G = [G11 G12;G21 G22];

    [W(:, :, nn+1), Q] = eig(F*G);
    Q = (sqrt(Q));
    qm = diag(Q);
    V(:, :, nn+1) = -G*W(:, :, nn+1)/Q;
    X(:, :, nn+1) = diag(exp(-k_0*qm*h_z(nn)))
        ;
end

```

```

% Eigenmatrices for reflection and transmission
layers
W(:, :, 1) = II;
W(:, :, N_1) = II;

VIxx = (1i/k_0)*diag((k_x_mn.*k_y_mn)./k_1_zmn);
VIxy = (1i/k_0)*diag((k_y_mn.^2 + k_1_zmn.^2)./
    k_1_zmn);
VIyx = -(1i/k_0)*diag((k_x_mn.^2 + k_1_zmn.^2)./
    k_1_zmn);
VIyy = -VIxx;
V(:, :, 1) = [VIxx VIxy;VIyx VIyy];
X(:, :, 1) = II;

VIIxx = (1i/k_0)*diag((k_x_mn.*k_y_mn)./k_3_zmn)
    ;
VIIxy = (1i/k_0)*diag((k_y_mn.^2 + k_3_zmn.^2)./
    k_3_zmn);
VIIyx = -(1i/k_0)*diag((k_x_mn.^2 + k_3_zmn.^2)
    ./k_3_zmn);
VIIyy = -VIIxx;
V(:, :, N_1) = [VIIxx VIIxy;VIIyx VIIyy];
X(:, :, N_1) = II;

% Eigenmatrices for the uncarved layers
for nn=1:3*NN_z
    if (mod(nn+1,3))==0
        k_n_zmn = k_m_zmn;
        D_n = D_m;
    else

```

```

        k_n_zmn = k_d_zmn;
        D_n = D_d;

    end

    W(:, :, 1+N_z+nn) = II;
    Vnxx = (1i/k_0)*diag((k_x_mn.*k_y_mn)./
        k_n_zmn);
    Vnxy = (1i/k_0)*diag((k_y_mn.^2 +
        k_n_zmn.^2)./k_n_zmn);
    Vnyx = -(1i/k_0)*diag((k_x_mn.^2 +
        k_n_zmn.^2)./k_n_zmn);
    Vnyy = -Vnxx;
    V(:, :, 1+N_z+nn) = [Vnxx Vnxy;Vnyx Vnyy];
    X(:, :, 1+N_z+nn) = diag(exp(-1i*[k_n_zmn;
        k_n_zmn]*D_n));

end

%% S matrix calculation

% Preallocating
Suu = II;
Sud = ZZ;
Sdu = ZZ;
Sdd = II;

for ll=1:N_l-1
    S = [W(:, :, ll+1) -W(:, :, ll);V(:, :, ll+1)
        V(:, :, ll)]\[W(:, :, ll)*X(:, :, ll) -W
        (:, :, ll+1)*X(:, :, ll+1);V(:, :, ll)*X
        (:, :, ll) V(:, :, ll+1)*X(:, :, ll+1)];

    % Cascade the next interface to the

```

```

        current S matrix
    Auu = Suu;
    Aud = Sud;
    Adu = Sdu;
    Add = Sdd;
    Buu = S(1:2*Nt,1:2*Nt);
    Bud = S(1:2*Nt,2*Nt+1:4*Nt);
    Bdu = S(2*Nt+1:4*Nt,1:2*Nt);
    Bdd = S(2*Nt+1:4*Nt,2*Nt+1:4*Nt);

    Suu = Buu*( (II-Aud*Bdu)\Auu);
    Sud = Bud+(Buu*Aud*( (II-Bdu*Aud)\Bdd));
    Sdu = Adu+(Add*Bdu*( (II-Aud*Bdu)\Auu));
    Sdd = Add*( (II-Bdu*Aud)\Bdd);

end

%% Efficiency

R_xy = u_x*Sdu(:,m0)+u_y*Sdu(:,Nt+m0);
T_xy = u_x*Suu(:,m0)+u_y*Suu(:,Nt+m0);

R_z = (k_x_mn./k_1_zmn).*R_xy(1:Nt) + (k_y_mn./
    k_1_zmn).*R_xy(Nt+1:2*Nt);
T_z = -(k_x_mn./k_3_zmn).*T_xy(1:Nt) - (k_y_mn./
    k_3_zmn).*T_xy(Nt+1:2*Nt);

R_xyz = [R_xy;R_z]; T_xyz = [T_xy;T_z];

DEri = real([ (k_1_zmn/k_1_zmn(m0)); (k_1_zmn/
    k_1_zmn(m0)); (k_1_zmn/k_1_zmn(m0)) ]).* (R_xyz
    .*conj(R_xyz));

```



```

DEti = real([(k_3_zmn/k_1_zmn(m0));(k_3_zmn/
            k_1_zmn(m0));(k_3_zmn/k_1_zmn(m0))]) .* (T_xyz
            .*conj(T_xyz));

DEr(yy,tt,ss) = sum(DEri(:));
DEt(yy,tt,ss) = sum(DEti(:));
[num2str(yy),'/',num2str(length(y)),' ',num2str
    (tt),'/',num2str(length(th))] % Display
    progress
            end
        end
    end

%% Plot

% Angular Spectrum
pp = 1; % Select the polarization for the plot in terms of psi(pp)
figure('Units','inches','Position',[5 2 6 5]);
h = pcolor(y/1000,th,(1-DEr(:,:,pp)-DEt(:,:,pp))');
set(h,'linestyle','none');
set(gca,'fontsize',20);
colormap('jet');
bb = colorbar;
bb.Label.String = 'Absorption';
bb.Label.Rotation = 270;
clims = get(gca,'clim');
bb.Label.Position = [3.75,(clims(1)+clims(2))/2,0];
caxis([0,1]);
xlabel('\lambda (\mum)');
ylabel('\theta (^o)');

```

```

% Line Plot
tt = 1; % [1,121,241]; % Incidence angles to be plotted in terms of th(
    tt)
figure('Units','inches','Position',[5 2 6 5]);
plot(y/1000,1-DEr(:,tt(1),pp)-DEt(:,tt(1),pp),'linewidth',2);
hold on
for aa=2:length(tt)
    plot(y/1000,1-DEr(:,tt(aa),pp)-DEt(:,tt(aa),pp),'-r','linewidth',2)
        ;
end
xlim([min(y),max(y)]/1000);
xlabel('\lambda (\mum)');
ylabel('Absorption');
title(['\psi = ',num2str(psi(pp)),'\circ']);
set(gca,'fontsize',20);
ylim([0,1]);
labels = cell(size(tt));
for aa=1:length(tt)
    labels(aa) = {'\theta = ',num2str(th(tt(aa)),'\circ'};
end
legend(labels);

```

Listing A.2: MATLAB script to recreate Fig. 5.7a

```

%% Inputs and Structure Parameters

y = 500; % Range of wavelength in nm

% Angles
th = 0; % Incidence Angle (deg)
phi = 0; % Angle between 'x' axis and plane of incidence (deg)
psi = 90; % Polarization angle (deg) 0 -> TM, 90 -> TE

```

```

% Unit cell parameters
mlt = 1; % Scaling factor for the hexagonal unit cell
D_x = 300; % Length of one period in 'x'
D_x = 2*round(D_x*mlt/2); % Scaled and rounded to nearest even number
D_y = 2*round(sqrt(3)*D_x/2); % Length of one period in 'y'

% Metal-dielectric metamaterials
D_m = 10; % Thickness of metal layer in 'z'
D_d = 30; % Thickness of dielectric layer in 'z'
NN_z = 6; % =10; for uncarved % Number of uncarved unit cells (after the
    moth-eyes)

% Moth-eye Structures
N_m = 4; % =0; for uncarved % Number of elementary cells carved into
    pillars
r_1 = 50*mlt; % Radius of pillars at top
r_2 = 145*mlt; % Radius of pillars at bottom
N_zd = 3; % Number of slices of the dielectric layer (calculates radius,
    increase for accuracy)
D_z = N_m*(2*D_d+D_m); % Thickness of moth-eye structure in 'z'
N_z = N_m*(2*N_zd+1); % Number of layers in one carved elementary cell
h_zd = D_d/N_zd; % Resolution in 'z' for carved dielectric layers
h_z = repmat([repmat(h_zd,1,N_zd),D_m,repmat(h_zd,1,N_zd)],1,N_m); %
    Height of each carved layer
z_1 = [0,cumsum(h_z(1:N_z-1))]; % 'z' coordinate of each carved layer
r_z = interp1([0,D_z-h_zd],[r_1,r_2],z_1); % Radius of pillars for each
    carved layer
N_l = N_z+3*NN_z+2; % Total layers

% Fourier modes to consider in calculations (ODD)

```

```

N_x = 9; %=1; for uncarved % Number of Fourier modes in x direction
N_y = 9; %=1; for uncarved % Number of Fourier modes in y direction
Nt = N_x*N_y;

% Preallocations
ky = 2*pi./y; % Wavenumbers
I = eye(Nt); II = eye(2*Nt); % Identity matrices
ZZ = zeros(2*Nt); zz = zeros(2*Nt,1);
EPS = zeros(Nt,Nt,N_1);
EPSyx = zeros(Nt,Nt,N_z);
EPSxy = zeros(Nt,Nt,N_z);
W = zeros(2*Nt,2*Nt,N_1);
V = zeros(2*Nt,2*Nt,N_1);
X = zeros(2*Nt,2*Nt,N_1);
qm = zeros(2*Nt,N_1);

% Foruier mode numbers and arrays
mx = (-(N_x-1)/2:(N_x-1)/2)';
my = (-(N_y-1)/2:(N_y-1)/2);
m0x = (N_x+1)/2;
m0y = (N_y+1)/2;
m0 = (Nt+1)/2;

%% Wavelength based permittivity

% Metal (with thin layer correction)
load Cu.txt; % Taken from refractiveindex.info
Me = interp1(Cu(:,1),Cu,y/1000); % Interpolation of experimental data
Metal = (Me(:,2) + 1i*Me(:,3)); Metal = Metal.';
kkk = D_m/39; % Thickness of W layer divided mean free path of W
kky = 1000*ky;

```

```

fi = (1./kkk+3/4*(1-1/12*kkk.^2).*expint(kkk)-3./(8*kkk.^2).* (1-exp(-kkk
    ))-(5./(8*kkk)+1/16-kkk/16).*exp(-kkk)).^-1;

wp = 6.5; % Plasma frequency in micron^-1
gamma = 12*10^-2; gammakk = gamma*fi/kkk;
epsDrude = 1-(wp^2)./((kky/(2*pi)).^2+1i*(kky/(2*pi))*gamma); % Drude
    model for the Bulk

epsDrudekk = 1-(wp^2)./((kky/(2*pi)).^2+1i*(kky/(2*pi))*gammakk); %
    Drude Model corrected for the thin layer

epsMetal = Metal-epsDrude+epsDrudekk;

%% Index profile of moth eye structures
% Build the moth-eye structure as a binary 3D matrix

indexProfLog = false(D_x,D_y,N_z);

% Hexagon vertice positions
centre = [D_x,D_y]/2;

for nn=1:N_z
    r = round(r_z(nn));
    % Pillars
    [rr,cc] = meshgrid(1:2*r+1);
    circ = (rr-1-r).^2+(cc-1-r).^2<=r^2;
    % Positioning the pillars
    indexProfLog((centre(1)-r):(centre(1)+r),(centre(2)-r):(centre(2)+r)
        ,nn) = circ;
    indexProfLog(1:r,1:r,nn) = indexProfLog(1:r,1:r,nn) | circ(r+2:2*r
        +1,r+2:2*r+1);

```

```

indexProfLog(1:r,D_y-r:D_y,nn) = indexProfLog(1:r,D_y-r:D_y,nn) |
    circ(r+2:2*r+1,1:r+1);
indexProfLog(D_x-r:D_x,D_y-r:D_y,nn) = indexProfLog(D_x-r:D_x,D_y-r:
    D_y,nn) | circ(1:r+1,1:r+1);
indexProfLog(D_x-r:D_x,1:r,nn) = indexProfLog(D_x-r:D_x,1:r,nn) |
    circ(1:r+1,r+2:2*r+1);
end

%% Structure Analysis

uy = y/1000; % Wavelength in micron

% Permittivity and refractive indices
n_1 = 1; % Refractive index of incidence medium
n_3 = sqrt(1 + 0.28604141 + 1.07044083/(1 - 1.00585997e-2/uy^2) + ...
    1.10202242/(1 - 100/uy^2)); % Refractive index for transmission
    medium (quartz)
e_m = epsMetal; % Permittivity of metal for current wavelength
e_d = 1 + 0.6961663/(1-(0.0684043/uy)^2) + ...
    0.4079426/(1 - (0.1162414/uy)^2) + 0.8974794/(1 - (9.896161/uy)
    ^2); % Permittivity of dielectric layer (SiO2)
e_f = 1; % Permittivity of material between pillars
e_p = repmat([repmat(conj(e_d),N_zd,1);conj(e_m);repmat(conj(e_d),N_zd
    ,1)],N_m,1);

% Permittivity matrices for each layer
indexProf = ones(D_x,D_y);
for nn=1:N_z
    indexProf(indexProfLog(:, :, nn)) = e_p(nn);
    indexProf(~indexProfLog(:, :, nn)) = e_f;
end

```

```

eps_fft = fftshift(fft2(indexProf))/(D_x*D_y);
eps_mn = eps_fft(D_x/2+2-N_x:D_x/2+N_x,D_y/2+2-N_y:D_y/2+N_y);

for pp = 1:N_x
    for qq = 1:N_y
        EE = rot90(eps_mn(pp:pp+N_x-1,qq:qq+N_y-1),2);
        EPS(pp+N_x*(qq-1),:,nn+1) = reshape(EE,1,[]);
    end
end

i_iepsx_mj = zeros(N_x,D_y,N_x);
iepsx_fft = fftshift(fft(indexProf.^(-1),[],1),1)/D_x;

for qq=1:D_y
    iepsx_m = iepsx_fft(D_x/2+2-N_x:D_x/2+N_x,qq);
    iepsx_mj = toeplitz(iepsx_m(N_x:2*N_x-1),flip(iepsx_m(1:N_x)));

    i_iepsx_mj(:,qq,:) = inv(iepsx_mj);
end

epsxy_fft = fftshift(fft(i_iepsx_mj,[],2),2)/D_y;
epsxy_mnj = epsxy_fft(:,D_y/2+2-N_y:D_y/2+N_y,:);

E4 = zeros(N_x,N_y,N_x,N_y);

for pp = 1:N_x
    for qq = 1:N_x
        E4(pp, :, qq, :) = toeplitz(epsxy_mnj(pp,N_y:2*N_y-1,qq),flip(
            epsxy_mnj(pp,1:N_y,qq)));
    end
end
end

```

```

EPSxy(:, :, nn) = reshape(E4, [N_x*N_y, N_x*N_y]);

i_iepsy_n1 = zeros(D_x, N_y, N_y);
iepsy_fft = fftshift(fft(indexProf.^(-1), [], 2), 2)/D_y;

for pp=1:D_x
    iepsy_n = iepsy_fft(pp, D_y/2+2-N_y:D_y/2+N_y);
    iepsy_n1 = toeplitz(iepsy_n(N_y:2*N_y-1), flip(iepsy_n(1:N_y)));

    i_iepsy_n1(pp, :, :) = inv(iepsy_n1);
end

epsyx_fft = fftshift(fft(i_iepsy_n1, [], 1), 1)/D_x;
epsyx_mn1 = epsyx_fft(D_x/2+2-N_x:D_x/2+N_x, :, :);

E4 = zeros(N_x, N_y, N_x, N_y);

for rr = 1:N_y
    for ss = 1:N_y
        E4(:, rr, :, ss) = toeplitz(epsyx_mn1(N_x:2*N_x-1, rr, ss), flip(
            epsyx_mn1(1:N_x, rr, ss)));
    end
end

EPSyx(:, :, nn) = reshape(E4, [N_x*N_y, N_x*N_y]);
end

%% Initializing variables
% Incident Field
u_x = cosd(psi)*cosd(phi)*cosd(th) - sind(psi)*sind(phi);

```



```

u_y = cosd(psi)*sind(phi)*cosd(th) + sind(psi)*cosd(phi);
inc = zz; inc(m0) = u_x; inc(Nt+m0) = u_y;

% Wavenumber Matrices
k_0 = ky;

k_xi = k_0*n_1*sind(th)*cosd(phi) + 2*pi*mx/D_x;
k_yi = k_0*n_1*sind(th)*sind(phi) + 2*pi*my/D_y;
k_x_mn = reshape(repmat(k_xi,1,N_y),[],1);
k_y_mn = reshape(repmat(k_yi,N_x,1),[],1);

k_1_zmn = conj(((n_1*k_0)^2*ones(Nt,1) - k_x_mn.^2 - k_y_mn.^2).^(1/2));
k_d_zmn = conj((e_d*(k_0)^2*ones(Nt,1) - k_x_mn.^2 - k_y_mn.^2).^(1/2));
k_m_zmn = conj((e_m*(k_0)^2*ones(Nt,1) - k_x_mn.^2 - k_y_mn.^2).^(1/2));
k_3_zmn = conj(((n_3*k_0)^2*ones(Nt,1) - k_x_mn.^2 - k_y_mn.^2).^(1/2));

K_x = 1i*diag(k_x_mn/k_0);
K_y = 1i*diag(k_y_mn/k_0);

%% Eigenmatrices
for nn=1:N_z
    % Eigenvalue formulation for the grating region
    F11 = -K_x*(EPS(:, :, nn+1)\K_y);
    F12 = I + K_x*(EPS(:, :, nn+1)\K_x);
    F21 = -I - K_y*(EPS(:, :, nn+1)\K_y);
    F22 = K_y*(EPS(:, :, nn+1)\K_x);
    F = [F11 F12; F21 F22];

    G11 = -K_x*K_y;
    G12 = EPSyx(:, :, nn) + K_x^2;
    G21 = -EPSxy(:, :, nn) - K_y^2;

```

```

G22 = K_x*K_y;
G = [G11 G12;G21 G22];

[W(:, :, nn+1), Q] = eig(F*G);
Q = (sqrt(Q));
qm(:, nn+1) = diag(Q);
V(:, :, nn+1) = -G*W(:, :, nn+1)/Q;
X(:, :, nn+1) = diag(exp(-k_0*qm(:, nn+1)*h_z(nn)));
end

% Eigenmatrices for reflection and transmission layers
W(:, :, 1) = II;
W(:, :, N_1) = II;

EPS(:, :, 1) = n_1^2*I;
VIxx = (1i/k_0)*diag((k_x_mn.*k_y_mn)./k_1_zmn);
VIxy = (1i/k_0)*diag((k_y_mn.^2 + k_1_zmn.^2)./k_1_zmn);
VIyx = -(1i/k_0)*diag((k_x_mn.^2 + k_1_zmn.^2)./k_1_zmn);
VIyy = -VIxx;
V(:, :, 1) = [VIxx VIxy;VIyx VIyy];
qm(:, 1) = 1i*[k_1_zmn;k_1_zmn]/k_0;
X(:, :, 1) = II;

EPS(:, :, N_1) = n_3^2*I;
VIIxx = (1i/k_0)*diag((k_x_mn.*k_y_mn)./k_3_zmn);
VIIxy = (1i/k_0)*diag((k_y_mn.^2 + k_3_zmn.^2)./k_3_zmn);
VIIyx = -(1i/k_0)*diag((k_x_mn.^2 + k_3_zmn.^2)./k_3_zmn);
VIIyy = -VIIxx;
V(:, :, N_1) = [VIIxx VIIxy;VIIyx VIIyy];
qm(:, N_1) = 1i*[k_3_zmn;k_3_zmn]/k_0;
X(:, :, N_1) = II;

```

```

% Eigenmatrices for the uncarved layers
for nn=1:3*NN_z
    if (mod(nn+1,3))==0
        k_n_zmn = k_m_zmn;
        D_n = D_m;
        EPS(:, :, 1+N_z+nn) = conj(e_m)*I;
    else
        k_n_zmn = k_d_zmn;
        D_n = D_d;
        EPS(:, :, 1+N_z+nn) = conj(e_d)*I;
    end
    W(:, :, 1+N_z+nn) = II;
    Vnxx = (1i/k_0)*diag((k_x_mn.*k_y_mn)./k_n_zmn);
    Vnxy = (1i/k_0)*diag((k_y_mn.^2 + k_n_zmn.^2)./k_n_zmn);
    Vnyx = -(1i/k_0)*diag((k_x_mn.^2 + k_n_zmn.^2)./k_n_zmn);
    Vnyy = -Vnxx;
    V(:, :, 1+N_z+nn) = [Vnxx Vnxy; Vnyx Vnyy];
    qm(:, 1+N_z+nn) = 1i*[k_n_zmn; k_n_zmn]/k_0;
    X(:, :, 1+N_z+nn) = diag(exp(-1i*[k_n_zmn; k_n_zmn]*D_n));
end

%% Big matrix calculation

% Preallocation
B = repmat(ZZ, 2*(N_l+1), 2*(N_l+1));

% Building B using b
for ll=1:N_l
    b = [W(:, :, ll) W(:, :, ll)*X(:, :, ll);
        V(:, :, ll) -V(:, :, ll)*X(:, :, ll)];
end

```

```

        -W(:, :, ll)*X(:, :, ll) -W(:, :, ll);
        -V(:, :, ll)*X(:, :, ll) V(:, :, ll)];

    B(4*(ll-1)*Nt+1:4*(ll+1)*Nt, 4*(ll-1)*Nt+1:4*ll*Nt) = b;
end

% The final two columns
b_l=[-W(:, :, 1), ZZ;
      V(:, :, 1), ZZ;
      repmat(ZZ, 2*(N_l-1), 2);
      ZZ, W(:, :, N_l);
      ZZ, V(:, :, N_l)];

B(:, 4*N_l*Nt+1:4*(N_l+1)*Nt) = b_l; % The BIG matrix

% Incident field matrix
Ein = inc;
Hin = V(:, :, 1)*Ein;
Fin = [Ein; Hin; repmat(zz, 2*N_l, 1)]; % Fields in each layer at incidence

C = B\Fin; % Column matrix with wave amplitudes for each layer

% Reflected and transmitted fourier modes
Cc = reshape(C, 4*Nt, N_l+1); % Rearrange
Cc(2*Nt+1:4*Nt, N_l) = zz; % Forcing incidence from transmission layer to
    0

R_xy = Cc(1:2*Nt, N_l+1);
T_xy = Cc(2*Nt+1:4*Nt, N_l+1);

%% Efficiency

```

```

R_z = (k_x_mn./k_1_zmn).*R_xy(1:Nt) + (k_y_mn./k_1_zmn).*R_xy(Nt+1:2*Nt)
    ;
T_z = -(k_x_mn./k_3_zmn).*T_xy(1:Nt) - (k_y_mn./k_3_zmn).*T_xy(Nt+1:2*Nt)
    );

R_xyz = [R_xy;R_z]; T_xyz = [T_xy;T_z];

DEri = real([(k_1_zmn/k_1_zmn(m0));(k_1_zmn/k_1_zmn(m0));(k_1_zmn/
    k_1_zmn(m0))]).*(R_xyz.*conj(R_xyz)));
DEti = real([(k_3_zmn/k_1_zmn(m0));(k_3_zmn/k_1_zmn(m0));(k_3_zmn/
    k_1_zmn(m0))]).*(T_xyz.*conj(T_xyz)));

DEr = sum(DEri(:));
DEt = sum(DEti(:));
Abs = 1-DEr-DEt

%% Fields

% Layer hieght array
h_l = [h_z, repmat([D_d,D_m,D_d],1,NN_z)];
% Layer permittivity array
eps_l = [n_1^2;e_p;repmat(conj([e_d;e_m;e_d]),NN_z,1);n_3^2];

% Space parameters
rz = 2; % Resolution in 'z'
zStart = -20; % Start plotting from this z coordinate
zEnd = sum(h_l) - zStart; % Stop plotting at this z coordinate
z = zStart:rz:zEnd;

rx = 5; % Resolution in 'x'
x = 1:rx:D_x-rx+1; % Need to compute just a single period

```

```

ry = 2; % Resolution in 'y'
y = D_y/2;

zi = 1; % Starting z index
ll = 1; % Starting layer

% z coordinate for the end of each layer
z_l = cumsum([0,h_l,Inf]);

% Preallocating field magnitude matrices
eps_z = zeros(length(x),length(y),length(z));
E_x = zeros(length(x),length(y),length(z));
E_y = zeros(length(x),length(y),length(z));
E_z = zeros(length(x),length(y),length(z));
H_x = zeros(length(x),length(y),length(z));
H_y = zeros(length(x),length(y),length(z));
H_z = zeros(length(x),length(y),length(z));
E_v = zeros(length(x),length(y),length(z),3);
H_v = zeros(length(x),length(y),length(z),3);
S_v = zeros(length(x),length(y),length(z),3);

while zi<=length(z)
    % Propagation in z
    if z(zi)<z_l(ll)
        p_z = exp(-k_0*qm(:,ll)*(z(zi)-z_l(ll-(ll~=1))));
        Phi_z = diag([p_z;X(:, :, ll)*p_z.^(-1)]);

        M = [W(:, :, ll), W(:, :, ll);
            EPS(:, :, ll)\[-K_y,K_x]*V(:, :, ll), -EPS(:, :, ll)\[-K_y,K_x]*V
            (:, :, ll)];

```

```

V(:, :, 11), -V(:, :, 11));
[-K_y, K_x]*W(:, :, 11), [-K_y, K_x]*W(:, :, 11)];

Psi_z = M*Phi_z*Cc(:, 11); % Field amplitude coefficients at
(*, *, z) in the incidence layer

for yi=1:length(y)
    p_y = exp(-k_0*diag(K_y)*y(yi)); % Propagation in x
    Phi_y = diag(repmat(p_y, 6, 1));

    Psi_yz = Phi_y*Psi_z; % Field amplitude coefficients at (*, y
    , z)
    for xi=1:length(x)
        p_x = exp(-k_0*diag(K_x)*x(xi)); % Propagation in x
        Phi_x = diag(repmat(p_x, 6, 1));

        Psi_xyz = Phi_x*Psi_yz; % Field amplitude coefficients
        at (x, y, z)

        % Separating the field components from \Psi(x, z)
        E_x(xi, yi, zi) = sum(Psi_xyz(1:Nt));
        E_y(xi, yi, zi) = sum(Psi_xyz(Nt+1:2*Nt));
        E_z(xi, yi, zi) = sum(Psi_xyz(2*Nt+1:3*Nt));
        H_x(xi, yi, zi) = sum(Psi_xyz(3*Nt+1:4*Nt));
        H_y(xi, yi, zi) = sum(Psi_xyz(4*Nt+1:5*Nt));
        H_z(xi, yi, zi) = sum(Psi_xyz(5*Nt+1:6*Nt));

        E_v(xi, yi, zi, :) = [E_x(xi, yi, zi), E_y(xi, yi, zi), E_z(xi, yi
        , zi)];
        H_v(xi, yi, zi, :) = [H_x(xi, yi, zi), H_y(xi, yi, zi), H_z(xi, yi
        , zi)];

```

```

        S_v(xi,yi,zi,:) = 0.5*real(cross(E_v(xi,yi,zi,:),conj(
            H_v(xi,yi,zi,:)));
        if(z(zi)<D_z && z(zi)>0)
            if(indexProfLog(round(x(xi)),round(y(yi)),ll-1))
                eps_z(xi,yi,zi) = eps_l(ll);
            else
                eps_z(xi,yi,zi) = e_f;
            end
        else
            eps_z(xi,yi,zi) = eps_l(ll);
        end
    end
end
    zi = zi + 1;
else
    ll = ll + 1;
end
end

%% Losses

absE2 = [];
imagEps = [];
absE2(:, :) = abs(E_x(:,1,:)).^2 + abs(E_y(:,1,:)).^2 + abs(E_z(:,1,:))
    .^2;
imagEps(:, :) = abs(imag(eps_z(:,1,:)));
ohmL = imagEps.*absE2;

%% Plot
figure('Units','inches','Position',[5 2 7 5]);
h = pcolor(z,x,ohmL);

```



```
set(h,'linestyle','none');
set(gca,'fontsize',20);
colormap('jet');
bb = colorbar;
bb.Label.String = 'Im(\epsilon)|E|^2';
bb.Label.Rotation = 270;
clims = get(gca,'clim');
bb.Label.Position = [3.5, (clims(1)+clims(2))/2, 0];
xlabel('z (nm)');
ylabel('x (nm)');

figure('Units','inches','Position',[5 2 7 5]);
h = pcolor(z,x,absE2);
set(h,'linestyle','none');
set(gca,'fontsize',20);
colormap('jet');
bb = colorbar;
bb.Label.String = '|E|^2';
bb.Label.Rotation = 270;
clims = get(gca,'clim');
bb.Label.Position = [3.75, (clims(1)+clims(2))/2, 0];
xlabel('z (nm)');
ylabel('x (nm)');
```

Bibliography

- [1] M. G. Moharam, E. B. Grann, D. A. Pommet, and T. K. Gaylord, “Formulation for stable and efficient implementation of the rigorous coupled-wave analysis of binary gratings,” *J. Opt. Soc. Am. A*, vol. 12, no. 5, pp. 1068–1076, 1995.
- [2] L. Li, “Formulation and comparison of two recursive matrix algorithms for modeling layered diffraction gratings,” *J. Opt. Soc. Am. A*, vol. 13, no. 5, pp. 1024–1035, 1996.
- [3] R. Morf, “Exponentially convergent and numerically efficient solution of Maxwell’s equations for lamellar gratings,” *J. Opt. Soc. Am. A*, vol. 12, no. 5, pp. 1043–1056, 1995.
- [4] E. Noponen and J. Turunen, “Eigenmode method for electromagnetic synthesis of diffractive elements with three-dimensional profiles,” *J. Opt. Soc. Am. A*, vol. 11, no. 9, pp. 2494–2502, 1994.
- [5] L. Li, “New formulation of the Fourier modal method for crossed surface-relief gratings,” *J. Opt. Soc. Am. A*, vol. 14, no. 10, pp. 2758–2767, 1997.
- [6] G. D’Aguanno, D. de Ceglia, N. Mattiucci, and M. J. Bloemer, “All-optical switching at the Fano resonances in subwavelength gratings with very narrow slits.” *Optics letters*, vol. 36, no. 11, pp. 1984–1986, 2011.
- [7] G. D’Aguanno, N. Mattiucci, M. J. Bloemer, D. de Ceglia, M. A. Vincenti, and

- A. Alù, “Transmission resonances in plasmonic metallic gratings,” *J. Opt. Soc. Am. B*, vol. 28, no. 2, pp. 253–264, 2011.
- [8] N. P. van der Aa and R. M. M. Mattheij, “Computing shape parameter sensitivity of the field of one-dimensional surface-relief gratings by using an analytical approach based on rcwa,” *J. Opt. Soc. Am. A*, vol. 24, no. 9, pp. 2692–2700, 2007.
- [9] G. D’Aguanno, N. Mattiucci, C. Conti, and M. J. Bloemer, “Field localization and enhancement near the Dirac point of a finite defectless photonic crystal,” *Phys. Rev. B*, vol. 87, no. 8, 085135, 2013.
- [10] F. Bloch, “Über die Quantenmechanik der Elektronen in Kristallgittern.” *Z. Physik*, vol. 52, no. 7-8, pp. 555–600, 1929.
- [11] G. Floquet, “Sur les équations différentielles linéaires à coefficients périodiques,” *Annales scientifiques de l’École Normale Supérieure*, vol. 12, pp. 47–88, 1883.
- [12] P. Lalanne and G. M. Morris, “Highly improved convergence of the coupled-wave method for TM polarization,” *J. Opt. Soc. Am. A*, vol. 13, no. 4, pp. 779–784, 1996.
- [13] L. Li, “Use of Fourier series in the analysis of discontinuous periodic structures,” *J. Opt. Soc. Am. A*, vol. 13, no. 9, pp. 1870–1876, 1996.
- [14] E. D. Palik, *Handbook of Optical Constants of Solids*. Academic Press, 1985.
- [15] W. Salisbury, “Absorbent body for electromagnetic waves,” U.S. Patent US2 599 944A, 1952.
- [16] V. G. Veselago, “The electrodynamics of substances with simultaneously negative values of ϵ and μ ,” *Soviet Physics Uspekhi*, vol. 10, no. 4, pp. 509–514, 1968.

- [17] R. A. Shelby, D. R. Smith, and S. Schultz, “Experimental verification of a negative index of refraction.” *Science*, vol. 292, no. 5514, pp. 77–79, 2001.
- [18] N. I. Landy, S. Sajuyigbe, J. J. Mock, D. R. Smith, and W. J. Padilla, “Perfect metamaterial absorber,” *Phys. Rev. Lett.*, vol. 100, no. 20, 207402, 2008.
- [19] H. Tao, N. I. Landy, C. M. Bingham, X. Zhang, R. D. Averitt, and W. J. Padilla, “A metamaterial absorber for the terahertz regime: design, fabrication and characterization,” *Optics Express*, vol. 10, no. 16, pp. 7181–7188, 2008.
- [20] X. Liu, T. Starr, A. F. Starr, and W. J. Padilla, “Infrared spatial and frequency selective metamaterial with near-unity absorbance,” *Phys. Rev. Lett.*, vol. 104, no. 20, 207403, 2010.
- [21] K. Aydin, V. E. Ferry, R. M. Briggs, and H. A. Atwater, “Broadband polarization-independent resonant light absorption using ultrathin plasmonic super absorbers,” *Nature Communications*, vol. 2, no. 517, 2011.
- [22] H. Wang and L. Wang, “Perfect selective metamaterial solar absorbers,” *Optics Express*, vol. 21, no. S6, pp. A1078–A1093, 2013.
- [23] C. Wu, B. Neuner, J. John, A. Milder, B. Zollars, S. Savoy, and G. Shvets, “Metamaterial-based integrated plasmonic absorber/emitter for solar thermophotovoltaic systems,” *Journal of Optics*, vol. 14, no. 2, 024005, 2012.
- [24] A. Ghanekar, L. Lin, and Y. Zheng, “Novel and efficient Mie-metamaterial thermal emitter for thermophotovoltaic systems,” *Optics Express*, vol. 24, no. 10, pp. A868–A877, 2016.
- [25] H. Yu, Z. Zhao, Q. Qian, J. Xu, P. Gou, Y. Zou, J. Cao, L. Yang, J. Qian, and Z. An,

- “Metamaterial perfect absorbers with solid and inverse periodic cross structures for optoelectronic applications,” *Optics Express*, vol. 25, no. 7, pp. 8288–8295, 2017.
- [26] N. Liu, M. Mesch, T. Weiss, M. Hentschel, and H. Giessen, “Infrared perfect absorber and its application as plasmonic sensor,” *Nano Letters*, vol. 10, no. 7, pp. 2341–2348, 2010.
- [27] K. Iwaszczuk, A. C. Strikwerda, K. Fan, X. Zhang, R. D. Averitt, and P. U. Jepsen, “Flexible metamaterial absorbers for stealth applications at terahertz frequencies,” *Optics Express*, vol. 20, no. 1, pp. 631–645, 2012.
- [28] Y. Shi, Y. C. Li, T. Hao, L. Li, and C. H. Liang, “A design of ultra-broadband metamaterial absorber,” *Waves in Random and Complex Media*, vol. 27, no. 2, pp. 381–391, 2017.
- [29] J. Zhu, Z. Ma, W. Sun, F. Ding, Q. He, L. Zhou, Y. Ma, and Citation:, “Ultra-broadband terahertz metamaterial absorber,” *Appl. Phys. Lett.*, vol. 105, no. 2, 021102, 2014.
- [30] N. Mattiucci, M. J. Bloemer, N. Aközbek, and G. D’Aguanno, “Impedance matched thin metamaterials make metals absorbing,” *Scientific Reports*, vol. 3, no. 3203, 2013.
- [31] Y. K. Zhong, Y.-C. Lai, M.-H. Tu, B.-R. Chen, S. M. Fu, P. Yu, and A. Lin, “Omnidirectional, polarization-independent, ultra-broadband metamaterial perfect absorber using field-penetration and reflected-wave-cancellation,” *Optics Express*, vol. 24, no. 10, pp. A832–A845, 2016.
- [32] N. Mattiucci, G. D’Aguanno, N. Akozbek, M. Scalora, and M. J. Bloemer, “Homogenization procedure for a metamaterial and local violation of the second principle of thermodynamics,” *Optics Communications*, vol. 283, no. 8, pp. 1613–1620, 2010.

- [33] H. A. Macleod, *Thin-Film Optical Filters, Fourth Edition*. CRC Press, 2010.
- [34] C. G. Bernhard and W. H. Miller, "A Corneal Nipple Pattern in Insect Compound Eyes," *Acta Physiologica Scandinavica*, vol. 56, no. 3–4, pp. 385–386, 1962.
- [35] D. Stavenga, S. Foletti, G. Palasantzas, and K. Arikawa, "Light on the moth-eye corneal nipple array of butterflies," *Proceedings of the Royal Society B: Biological Sciences*, vol. 273, no. 1587, pp. 661–667, 2006.
- [36] S. Chattopadhyay, Y. F. Huang, Y. J. Jen, A. Ganguly, K. H. Chen, and L. C. Chen, "Anti-reflecting and photonic nanostructures," *Materials Science and Engineering R*, vol. 69, no. 1–3, pp. 1–35, 2010.
- [37] R. J. Weiblen, C. R. Menyuk, L. E. Busse, L. B. Shaw, J. S. Sanghera, and I. D. Aggarwal, "Optimized moth-eye anti-reflective structures for As_2S_3 chalcogenide optical fibers," *Optics Express*, vol. 24, no. 10, pp. 10 172–10 187, 2016.
- [38] G. Tan, J.-H. Lee, Y.-H. Lan, M.-K. Wei, L.-H. Peng, I.-C. Cheng, and S.-T. Wu, "Broadband antireflection film with moth-eye-like structure for flexible display applications," *Optica*, vol. 4, no. 7, pp. 678–683, 2017.
- [39] S. Y. Chou, P. R. Krauss, and P. J. Renstrom, "Nanoimprint lithography," *Journal of Vacuum Science & Technology B*, vol. 14, no. 6, pp. 4129–4133, 1996.
- [40] M. Kowalczyk, J. Haberko, and P. Wasylczyk, "Microstructured gradient-index antireflective coating fabricated on a fiber tip with direct laser writing," *Optics Express*, vol. 22, no. 10, pp. 12 545–12 550, 2014.
- [41] M. A. Ordal, R. J. Bell, R. W. Alexander, L. L. Long, and M. R. Querry, "Optical properties of Au, Ni, and Pb at submillimeter wavelengths," *Applied Optics*, vol. 26, no. 4, pp. 744–752, 1987.

- [42] E. Sondheimer, “Advances in Physics The mean free path of electrons in metals,” *Advances in Physics*, vol. 1, no. 1, pp. 1–41, 1952.
- [43] C. Z. Tan, “Determination of refractive index of silica glass for infrared wavelengths by IR spectroscopy,” *Journal of Non-Crystalline Solids*, vol. 223, no. 1-2, pp. 158–163, 1998.
- [44] T. J. Bright, J. I. Watjen, Z. M. Zhang, C. Muratore, A. A. Voevodin, . C. Muratore, D. I. Koukis, D. B. Tanner, and D. J. Arenas, “Infrared optical properties of amorphous and nanocrystalline Ta₂O₅ thin films Infrared optical properties of amorphous and nanocrystalline Ta₂O₅ thin films,” *Journal of Applied Physics*, vol. 114, no. 8, 083515, 2013.